

## ABSTRACT

WAN, YANJUN. Simple Molecule Mercury Sensor. (Under the direction of Dr. Christopher B. Gorman.)

Several molecules previously produced from a nitrile-based cascade cyclization were examined as potential mercury sensors. Various analytical parameters, including fluorescence quantum yield, UV shift, fluorescence quenching, binding constant, binding ratio, and lowest detection limit, were measured. The best mercury sensor molecule was found to be molecule **3c**, which could be easily synthesized in gram quantities (3 steps, 55% overall yield). This molecule has a very high fluorescence quantum yield ( $\Phi = 0.87$ ), high sensitivity and selectivity towards mercury ion in both organic and aqueous media. The overall performance of molecule **3c** is as good as, or better than, the majority of organic dye based mercury sensors reported to date.

# Simple Molecule Mercury Sensor

by  
Yanjun Wan

A thesis submitted to the Graduate Faculty of  
North Carolina State University  
In partial fulfillment of the  
Requirements for the degree of  
Master of Science

Chemistry

Raleigh, North Carolina

2008

APPROVED BY:

---

Christopher Gorman  
Committee Chair

---

Edmond Bowden

---

Stefan Franzen

---

David Shultz

# DEDICATION

Seek first his kingdom and his righteousness, and all these things will be given to you as well.

– *Matthew 6:33*

## **BIOGRAPHY**

YanJun Wan was born in China in the year of 1983. She attended elementary school, middle school, and high school in China, and graduated high school with straight As. After high school, YanJun attended Shanghai Jiao Tong University. In June 2005, YanJun graduated from Shanghai Jiao Tong University with a Bachelor of Science degree in Chemistry, and a Bachelor of Arts degree in Finance as double-major. To further her knowledge in Chemistry, YanJun decided to go to graduate school at North Carolina State University, where she pursued a Master of Science degree in Chemistry under the direction of Dr. Christopher B. Gorman.

## ACKNOWLEDGMENTS

I would like to first thank my parents for their love and support, despite of the distance between us. I would also like to thank Berk and Barbara Wilson, who are like my parents in Raleigh, for bringing light to my life, and teaching me the righteous way of living through life's up-and-downs, and for their constant love, care, and encouragement.

I would like to thank Dr. Christopher B. Gorman for being the most wonderful advisor I could ever imagine. He taught me not just Chemistry, but a whole series of life philosophy, which is eventually even more important than Chemistry; when I look back, working for him is one of my wisest decisions in life. I would also like to thank all members in my Advisory Committee, Dr. Edmond Bowden, Dr. Stefan Franzen, and Dr. David Shultz, for always being available and patient whenever I have any questions. I would like to thank the Gorman Group. Every single one of them has always been helpful and encouraging to me. It was my pleasure to be able to work with them. I would also like to thank Dr. Paul Boyle for X-ray Structure Analysis, Dr. Matthew Lynton for Mass Spectroscopy Analysis, Dr. Lin He for suggestions on fluorescence measurements. The Mercury Sensor Project was supported by US Department of Energy (Grant DE-FG02-05ER46238). The Molecular Transistor Project was supported by National Science Foundation (DMR-0303746).

I would like to thank my "brothers and sisters" in Raleigh, Sasha Movchan, Susan Pope, and Alina Efremenko, for always being there when I cry or when I laugh, and for loving me and always supporting me in front of others, yet never hesitating to point out my faults privately. I would also like to thank my church - Grace Community Church.

# TABLE OF CONTENTS

<b>LIST OF TABLES .....</b>	<b>vi</b>
<b>LIST OF FIGURES .....</b>	<b>vii</b>
<b>LIST OF SCHEMES .....</b>	<b>ix</b>
<b>INTRODUCTION .....</b>	<b>1</b>
1.1 The Importance of Mercury Sensing .....	2
1.2 Four Major Categories of Mercury Sensors .....	2
1.3 Organic Dye Based Mercury Sensors –Advantages and Challenges .....	7
<b>A SMALL MOLECULE MERCURY SENSOR.....</b>	<b>9</b>
2.1 Introduction.....	10
2.2 Results and Discussion .....	11
2.3 Conclusions .....	24
2.4 Experimental Section.....	27
<b>MOLECULAR TRANSISTOR PROJECT .....</b>	<b>33</b>
3.1 Introduction.....	34
3.2 Results and Discussion .....	37
3.21 Synthesis and Characterization of Linker Molecules .....	37
3.22 Synthesis of Metal and Metal Oxide Nanoparticles .....	39
3.23 Ligand Exchange Experiments .....	39
3.3 Conclusion .....	43
3.4 Prospects for Synthesis of Nanoparticle Hetero-dimers and Hetero-trimers.....	43
3.5 Experimental Section.....	51
<b>REFERENCES .....</b>	<b>62</b>

## LIST OF TABLES

<b>Table 1.</b> A summary of recently reported mercury sensors.....	3
<b>Table 2.</b> Photophysical data for <b>3b</b> , <b>3c</b> , <b>5b</b> , and <b>5c</b> .....	14
<b>Table 3.</b> Different base systems for invariant concentration Job plot.....	17
<b>Table 4.</b> Binding constant $K_a$ of molecule <b>3c</b> to different metal cations, calculated by Benesi-Hildebrand plot.....	21
<b>Table 5.</b> A quantitative comparison of molecule <b>3c</b> to other promising organic dye based mercury sensors.....	25
<b>Table 6.</b> Minimum linker lengths by calculation versus available linker lengths.....	48

## LIST OF FIGURES

<b>Figure 1.</b> X-ray crystal structures of <b>3b</b> , <b>3c</b> , <b>5b</b> , and <b>5c</b> .	12
<b>Figure 2.</b> Photograph of solutions of 0.1mM <b>3b</b> , <b>3c</b> , <b>5b</b> , and <b>5c</b> under UV light.	13
<b>Figure 3.</b> Electronic absorption spectra of <b>3b</b> , <b>3c</b> , <b>5b</b> , and <b>5c</b> in acetonitrile.	14
<b>Figure 4.</b> Fluorescence quantum yield calculation for <b>3b</b> , <b>5b</b> , <b>3c</b> , and <b>5c</b> in acetonitrile.	14
<b>Figure 5.</b> 0.5 mM molecule <b>3c</b> mixed with 0.5 mM different metal cations, in 1% 0.2 M phosphate buffer and 99% acetonitrile. a) under day light; b) under UV lamp.	15
<b>Figure 6.</b> Invariant concentration Job plot of molecule <b>3c</b> to mercury in acetonitrile.	16
<b>Figure 7.</b> Invariant concentration Job plot of molecule <b>3c</b> to mercury in 1% aqueous buffer and 99% acetonitrile.	18
<b>Figure 8.</b> Suggested structure of the complex formed between molecule <b>3c</b> and mercury nitrate.	18
<b>Figure 9.</b> A similar mercury complex characterized by X-ray diffraction by Ancker, et al. <sup>20</sup>	19
<b>Figure 10.</b> Binding of molecule <b>3c</b> to mercury shows an obvious red shift upon increasing mercury concentration, in 0.5% 0.1 M phosphate buffer and 99.5% acetonitrile.	20
<b>Figure 11.</b> Addition of molecule <b>3c</b> to mercury solution, where the concentration of mercury solution stays at 1 mM, while the concentration of molecule <b>3c</b> solution varies from 0 to 50 $\mu$ M. Solvent: 2% 0.25 M phosphate buffer and 98% acetonitrile.	20
<b>Figure 12.</b> Benesi-Hildebrand plot reveals the binding constant between molecule <b>3c</b> and mercury: $K_a = 4.94 \times 10^4 \text{ M}^{-1}$ .	21
<b>Figure 13.</b> Structure comparison between molecule <b>3c</b> and isoquinoline-3-amine.	22
<b>Figure 14.</b> Binding constant comparison between molecule <b>3c</b> and isoquinoline-3-amine in 0.5% 0.1M phosphate buffer and 99.5% acetonitrile. Addition of molecule <b>3c</b> incurred an obvious peak at 400 nm, but the same concentration of isoquinoline-3-amine did not incur any peak at 400 nm.	22
<b>Figure 15.</b> Oxygen dependent fluorescence quenching of molecule <b>3c</b> . Flushing oxygen for 15 seconds reduced more than half of the fluorescence of molecule <b>3c</b> , this quenching is reversible and the fluorescence of molecule <b>3c</b> can be recovered upon flushing nitrogen.	23
<b>Figure 16.</b> Available thiophene molecules for future examination.	26
<b>Figure 17.</b> Proposed structures of water-soluble versions of molecule <b>3c</b> .	27
<b>Figure 18.</b> A cartoon of the definition of (from left to right) homo-dimer, hetero-dimer, homo-trimer, and hetero-trimer.	35
<b>Figure 19.</b> a) TEM image of 7 nm iron oxide nanoparticles; b) Histogram of the size distribution of nanoparticles in a).	39
<b>Figure 20.</b> TEM images of iron oxide nanoparticle samples after ligand exchange with tartaric acid, showing (left) aggregated particles and (right) debris thought to result from aggregates of excess ligand that were not removed upon purification.	41
<b>Figure 21.</b> a) TEM image of 3nm gold nanoparticles capped by hexanethiol; b) Histogram of the size distribution of nanoparticles in a); c) TEM image of 3nm platinum nanoparticles capped by hexanethiol; d) Histogram of the size distribution of nanoparticles in c).	42
<b>Figure 22.</b> Minimum linker length calculation for gold-iron oxide hetero-dimer.	45

**Figure 23.** (a) The minimum linker length calculation for gold homo-trimer; (b) Structure and length of available three-arm homo-linker..... 46

**Figure 24.** (a) The minimum linker length calculation for gold-iron oxide hetero-trimer; (b) Structure and lengths of the proposed three-arm hetero-linker. .... 47

**Figure 25.** Figure from reference paper: schematic drawing showing the current flow through homo-dimer.<sup>41</sup> ..... 51

## LIST OF SCHEMES

<b>Scheme 1.</b> Synthesis of oligomer precursors. ....	11
<b>Scheme 2.</b> Cascade closure of multiple aromatic rings.....	12
<b>Scheme 3.</b> Synthetic routes to four target linker molecules.....	38

# Chapter 1

---

## **INTRODUCTION**

## **1.1 The Importance of Mercury Sensing**

There is an increasing concern over the severe risk of heavy metal pollution and poisoning in environment, food, and products.<sup>1</sup> Mercury ion is of particular interest because of its high toxicity and its ability to cause a wide variety of damage to the kidneys, digestive system, and neurological system.<sup>2</sup> Different forms of mercury can also be transformed between one another, under different environmental conditions.<sup>3</sup> The most harmful form – methylated mercury, can become biomagnified up the food chain, reaching  $10^6 - 10^7$  times greater in some fish species, compared to the amount in surrounding water.<sup>4</sup> Such high mercury levels can affect the health of animals at all stages in the food chain, including humans.<sup>3</sup> Thus, a simple yet highly-selective routine to detect mercury ions in both organic and aqueous media is of great interest.

## **1.2 Four Major Categories of Mercury Sensors**

Most recently developed mercury sensors fall into one of four general categories: nano-particle based sensors, DNA or other bio-molecule based sensors, polymer based sensors, or organic dye based sensors. Table 1 summarizes several of these and indicates potential advantages and disadvantages of each.

**Table 1.** A summary of recently reported mercury sensors.

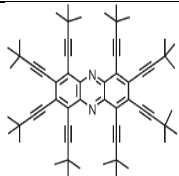
Ref	Structure	Synthetic Steps & Overall Yield	Detection Method	Binding Constant $\log K_a$	Range of Detection /Detection Limit	Pros	Cons
5		4 steps, 18% yield	UV, Fluorescence	“attempts to obtain $K_a$ to $Hg(OTf)_2$ were inconclusive”	NR*	“the synthesis of the first representatives of the heteroacenes”	Sensor gives the same signal to $Hg^{2+}$ , $Ag^+$ , and $As^{3+}$ .
6	3-mercaptopropionic acid-functionalized gold nanoparticles	NA**	Colorimetric, UV, TEM, DFS (optical dark-field scattering)	NR*	3.0nM sensor detects 1.0mM $Hg^{2+}$ or 50mM sensor detects 0.1mM $Hg^{2+}$ by colorimetric method; theoretical calculation (signal : noise ratio = 3 : 1) of lowest detection limit is 50mM sensor detects 0.1 $\mu$ M $Hg^{2+}$ .	Aqueous and colorimetric method of detection.	AuNP sensor is very susceptible towards pH, buffer species, capping ligand, chelating ligand, etc. If any of them is not controlled exactly, the sensor will have a very poor selectivity towards many other metal cations.

Table 1 continued...

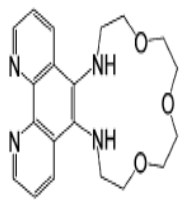
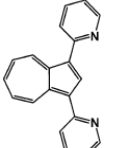
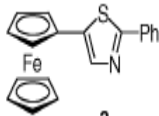
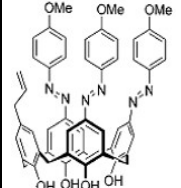
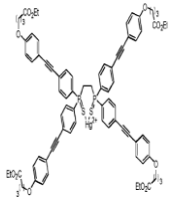
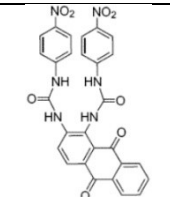
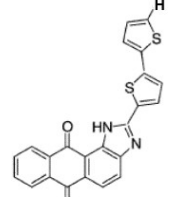
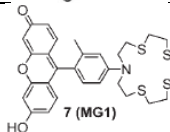
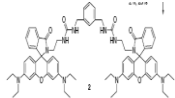
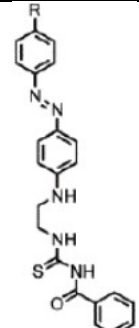
7		2 steps, 1.8% yield	UV, Luminescence, <sup>1</sup> H-NMR	7.84 by UV, 7.76 by emission	NR*	High binding constant; and the binding constants calculated from UV and emission are very close. Nice binding ratio figure showing the 1:1 sensor: Hg <sup>2+</sup> binding.	Also gives high binding constants (log K <sub>a</sub> up to 4.61) towards several other metal cations.
8		6 steps, 12% yield	Colorimetric, UV, NMR	NR*	~0.05-1mM	Obvious color change (red to blue).	Gives the same color change to Pb <sup>2+</sup> , Cu <sup>2+</sup> , Cr <sup>3+</sup> , and CF <sub>3</sub> COOH, besides Hg <sup>2+</sup> .
9		2 steps, 34% yield	Colorimetric, UV	3.58	~1mM	Obvious color change (red to yellow).	Gives the same color change and binding constant K <sub>a</sub> to both Hg <sup>2+</sup> and Pb <sup>2+</sup> .
10		4 steps, 12-24% yield	Colorimetric, UV, <sup>1</sup> H-NMR	8.35	~10μM	Obvious color change (light yellow to red).	Gives the same color change to Cr <sup>3+</sup> , Ni <sup>2+</sup> , Cu <sup>2+</sup> , Ag <sup>+</sup> , Cd <sup>2+</sup> , Hg <sup>+</sup> , and Pb <sup>2+</sup> , besides Hg <sup>2+</sup> .

Table 1 continued...

2		2 steps, 24% yield	UV, Fluorescence	8.4	Data range is ~1μM, theoretical calculation (when signal-to-noise ratio is 3) of lowest detection limit is 3.8nM.	Aqueous medium. Nice contrast-competition study.	Binding constant log $K_a$ of $Ag^+$ is 4.6; sensor only works under specific pH value (pH = 4).
11		2 steps, 46% yield	UV	$K_a = 4.2$ $\times 10^5$	~50μM	Can separate $Hg^{2+}$ from other metal cations examined in this paper.	Other metal cations give up to 1/4 signal of that of $Hg^{2+}$ .
12		1-2 steps, 41-92% yield	Colorimetric, UV, Fluorescence	0.1243	NR*		Give a close log $K_a$ on other metal cations examined.
13		4 steps, 5% yield	Fluorescence	NR*	Up to 0.03ppm (0.15μM)	Aqueous, binding with $Hg^{2+}$ increases fluorescence by 44 fold, instead of quenching it.	Only works under a specific pH (pH = 7); 5 step synthesis with an overall yield of 5%.

**Table 1 continued...**

14	DNA-Au NPs	NA**	Colorimetric, Melting curve ( $T_m$ )	NR*	Up to 100nM (20ppb) by naked eyes	Lowest reported colorimetric detection limit.	DNA is very susceptible towards temperature, pH, salts, etc.
15	Water-soluble polymer + mercury-specific oligonucleotide	NA**	Colorimetric, UV, Fluorescence	NR*	12.5 $\mu$ M by naked eyes, 2.5 $\mu$ M by UV, 42nM by fluorescence	Aqueous, other cations examined did not give color change.	Polymer sensor might be susceptible towards different experimental conditions.
16		2 steps, 18% yield	Colorimetric, Fluorescence	$K_a = 3.2 \times 10^5$	0.3mM by naked eyes	Only $Zn^{2+}$ gave slight response among all metal cations examined.	Low sensitivity (high detection limit).
17		2 steps, 23-39% yield	Colorimetric, UV	NR*	20 $\mu$ M by naked eyes	Aqueous.	Only valid in pH range of 4-9; difficult synthesis with an overall yield of 23-39% (depending on different R).

NR\* = Not Reported.

NA\*\* = Not Applicable. Only organic-dye based sensors have corresponding synthetic steps and overall yields.

While sensors in the first three categories usually have the advantage of lower detection limit, their applications are highly constrained by their susceptibility to a series of factors, including temperature, pH, and other salts. For example, DNA-functionalized gold nanoparticles described by Lee, et al., showed the lowest reported colorimetric detection limit of 100 nM (20 ppb) in aqueous media.<sup>14</sup> However, two important components of this sensor, DNA and gold nanoparticles, are both known to show a large variability in their behavior as a function of temperature, pH, and the presence of other salts. In fact, the whole detection process required a thermal controller to control temperature between 46 °C to 50 °C. Another example is the mercury sensor reported by Liu, et al., which used a water-soluble conjugated polymer and a label-free, mercury-specific oligonucleotide probe.<sup>15</sup> This sensor can detect different concentration ranges of mercury by different means – it has an aqueous detection limit of 12.5 μM by colorimetric detection, 2.5 μM by UV, and 42 nM by fluorescence. However, due to the sensitive and fragile nature of the polymer and the probe, this sensor can hardly serve as an inexpensive way of detecting different forms of mercury in a variety of environments.

### **1.3 Organic Dye Based Mercury Sensors –Advantages and Challenges**

Unlike sensors in the first three categories, organic dye based sensors are usually synthesized organic molecules with high fluorescence and remarkable optical changes upon binding to mercury ions, with the potential advantages of low cost, easy storage, and better tolerance of different environmental conditions. Despite of these advantages, organic dye

based mercury sensors usually suffer from one or several disadvantages, including multi-step synthesis with low overall yield; poor sensitivity and/or selectivity; low binding constant; and poor aqueous solubility.

Some of the most convincing and potentially useful organic dye based mercury sensors are: Mercury Green 1 synthesized by Yoon, et al., with a quantum yield of 0.72, and a detection limit up to 0.03 ppm (0.15  $\mu\text{M}$ ) in aqueous medium;<sup>13</sup> and azo-component containing chemodosimeters synthesized by Lee, et al., with a colorimetric detection limit of 4 ppm (20  $\mu\text{M}$ ) by naked eyes in aqueous medium.<sup>17</sup> Unfortunately, both sensors require considerable amount of effort in synthesis, and are limited to use only in specific pH ranges. Other various organic dye based sensors cited in Table 1 all have different drawbacks as well. Some sensor molecules require long synthetic routes, and the overall yields are less than 20%.<sup>5,7,9,16</sup> Some sensor molecules are poor at differentiating mercury from other metal ions, most commonly, zinc, cadmium, lead, copper, silver, etc.<sup>5,7-10</sup> On top of these drawbacks, most organic dye based sensors can only detect mercury ions in organic solution.<sup>5,7-12</sup> For the few molecules that are claimed to be able to respond to aqueous mercury, experiments were performed in mixed solvent systems (usually acetonitrile : water or dimethylsulfoxide : water).<sup>2,17</sup>

Thus, although many mercury sensing molecules and assemblies have been reported, none is universally applicable or ideal. This lack has prompted the study of other molecules that respond to mercury. Such a study is reported in the next chapter of this thesis.

## Chapter 2

---

### **A SMALL MOLECULE MERCURY SENSOR**

## 2.1 Introduction

For an organic dye based mercury sensor to be applicable in industry, the common challenges listed in Chapter 1 have to be addressed properly. First of all, an easy synthetic route for large scale synthesis with a decent overall yield is a must for industrial application. Second, high selectivity of the sensor, especially the ability to differentiate mercury from other commonly present metal cations, is also crucial. Third, a sensor that could detect mercury ions in both organic and aqueous media would be highly preferred. Besides these, high binding constant and low detection limit are also key parameters of the overall performance. A large detection range and variety in detection methods (e.g. colorimetric, UV, fluorescence, etc) are also helpful.

Our group recently discovered a new methodology to close multiple aromatic rings in nitrile-containing oligomers in a cascade cyclization. This methodology involves the synthesis of a series of nitrile-containing precursor oligomers, the acid-catalyzed cyclization that are widely reported in the synthesis of isoquinolines,<sup>18</sup> followed by the spontaneous tautomerization of CH groups to NH groups. To our knowledge, this new methodology is the first to report cascade closure of multiple aromatic rings. A series of products synthesized by this methodology exhibit high quantum yield, which can potentially be used as organic dye based sensors for different heavy metal ions.

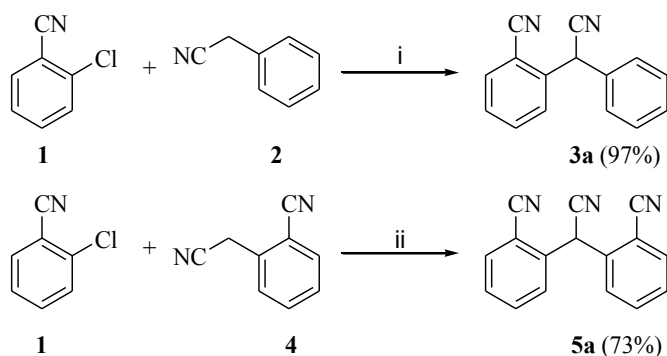
Presented below are several potential organic dye based mercury sensors (**3b**, **3c**, **5b**, and **5c**) synthesized by this cascade cyclization methodology, and their performance as colorimetric sensors. Their electronic absorption spectra and quantum yield were examined and molecule **3c** was chosen for further study. Then a qualitative colorimetric experiment

revealed the high selectivity of molecule **3c** towards mercury ion, and a series of quantitative measurements, including UV shift, fluorescence quenching, binding ratio, binding constant, and lowest detection limit in both organic and aqueous media, were performed to examine the overall performance of molecule **3c** as a potential mercury sensor.

## 2.2 Results and Discussion

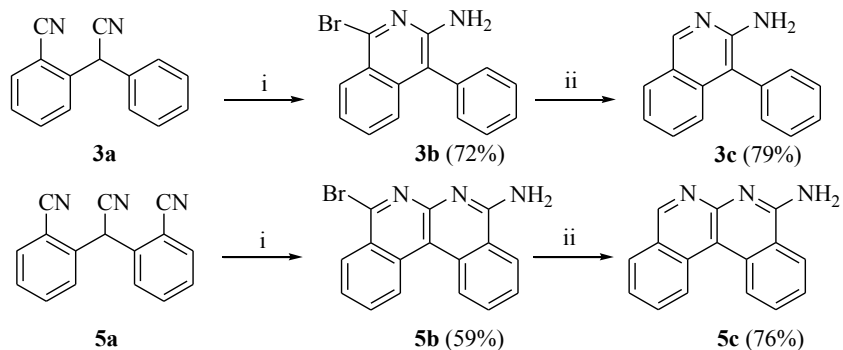
As shown in Scheme 1, oligomers **3a** and **5a** can be easily synthesized from commercially available starting materials. These oligomers could then be converted to cyclized products (Scheme 2) in which the benzylic CH groups were found to tautomerize to NH. This process results in entirely aromatic rings. To our knowledge, this is the first example of cyclization/aromatization of this kind. Full details of every synthetic step are provided in the experimental section.

**Scheme 1.** Synthesis of oligomer precursors.



*i) KOtBu, DMF, rt, 1h; ii) KOtBu, DMF, 70 °C, 18h*

**Scheme 2.** Cascade closure of multiple aromatic rings.



*i) HBr/HOAc; ii) NaBH<sub>4</sub>, Pd on Carbon*

Crystals of **3b**, **3c**, **5b**, and **5c**, suitable for X-ray diffraction, were obtained by group member Weijun Niu (Figure 1). These data showed that we were able to close multiple aromatic rings in one step reaction, followed by debromination to reduce considerable steric hindrance.

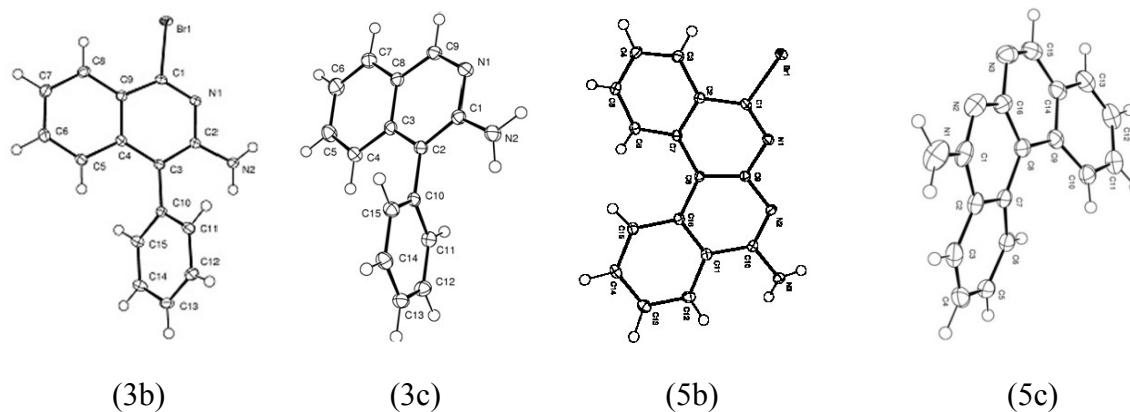


**Figure 1.** X-ray crystal structures of **3b**, **3c**, **5b**, and **5c**.

In Figure 2, solutions of **3b**, **3c**, **5b**, and **5c** at the same concentration (0.1 mM, in acetonitrile) showed considerable differences in fluorescence under UV lamp - the debrominated **3c** and **5c** showed obviously higher fluorescence. For a sensor to operate via fluorescence quenching, a large quantum yield of fluorescence in the unbound form, and a small quantum yield in the mercury bound form is desirable.

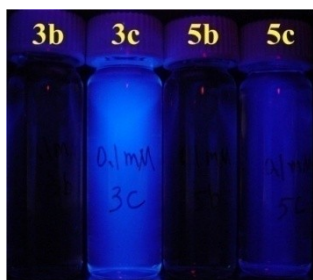


**Figure 2.** Photograph of solutions of 0.1mM **3b**, **3c**, **5b**, and **5c** under UV light.

The electronic absorption spectra of these 4 molecules are shown in Figure 3. One can see that molecule **5c** has a slightly higher extinction coefficient at virtually all wavelengths than other molecules. The quantum yields for fluorescence were determined in anhydrous acetonitrile, between 375 nm and 600 nm. The results are shown in Figure 4 and Table 2. Molecule **3c** gave approximately 5 times higher quantum yield than molecule **5c**. Based on quantum yield, molecule **3c** was chosen as the most promising sensor for heavy metal ions among these molecules. Detailed procedures for obtaining electronic absorption spectra and measuring quantum yields are provided in the experimental section.

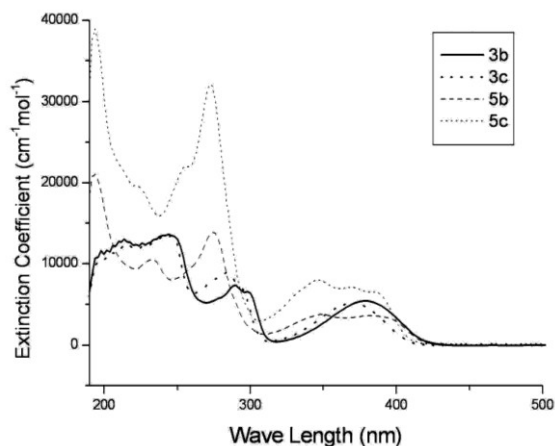


**Figure 3.** Electronic absorption spectra of **3b**, **3c**, **5b**, and **5c** in acetonitrile.

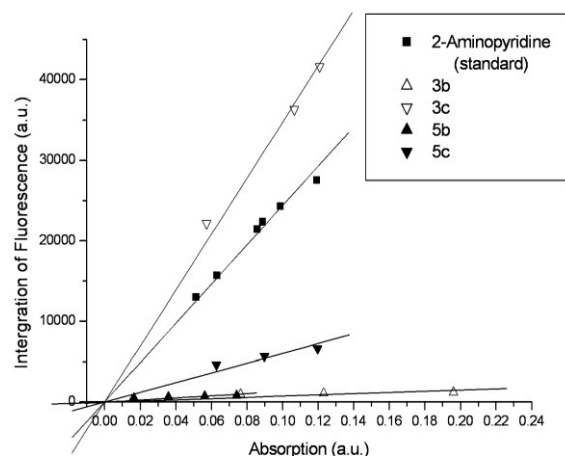


**Figure 4.** Fluorescence quantum yield calculation for **3b**, **5b**, **3c**, and **5c** in acetonitrile.

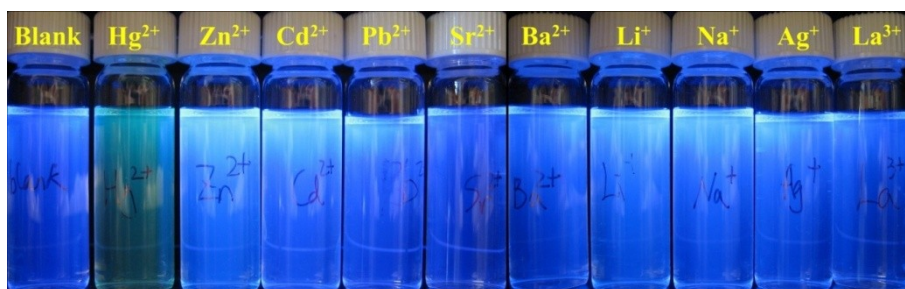
**Table 2.** Photophysical data for **3b**, **3c**, **5b**, and **5c**.

Compound	Abs. Max	Fl. Max	Φ (Quantum Yield)
3b	378nm	447nm	2%
3c	370nm	436nm	<b>87%</b>
5b	348nm	450nm	3%
5c	346nm	432nm	15%

In qualitative tests, molecule **3c** exhibited very high selectivity towards mercury ion. In Figure 5a, the vial with mercury nitrate showed an obvious color change from colorless to dark yellow, while in Figure 5b, the vial with mercury nitrate showed almost completely quenching of the fluorescence of molecule **3c**. No other metal cations examined here exhibited the same color change or fluorescence quenching, qualitatively suggesting a high selectivity of molecule **3c** towards mercury ion.



(a)



(b)

**Figure 5.** 0.5 mM molecule **3c** mixed with 0.5 mM different metal cations, in 1% 0.2 M phosphate buffer and 99% acetonitrile. a) under day light; b) under UV lamp.

To determine the stoichiometry of the molecule/mercury complex, an X-ray diffraction showing the crystal structure of the molecule/mercury complex would be most desirable. However, due to the low solubility and stability of the molecule/mercury complex in common solvents, several attempts to obtain crystals suitable for X-ray diffraction were all unsuccessful. Thus, an invariant concentration Job plot (Figure 6) was constructed. In this plot, the absorbance of a series of acetonitrile solutions with the same total concentration, but different ratios of molecule **3c** to mercury, were measured. These absorptions were then plotted versus the concentration fraction of molecule **3c**. The peak of this plot corresponds to

complete binding of all molecule **3c** and all mercury ions available in solution. Solving  $[\mathbf{3c}] / ([\mathbf{3c}] + [\text{Hg}^{2+}]) = 0.65$  gives the ratio of  $[\mathbf{3c}]:[\text{Hg}^{2+}] = 2:1$ , indicating a 2:1 stoichiometry of the molecule/mercury complex.

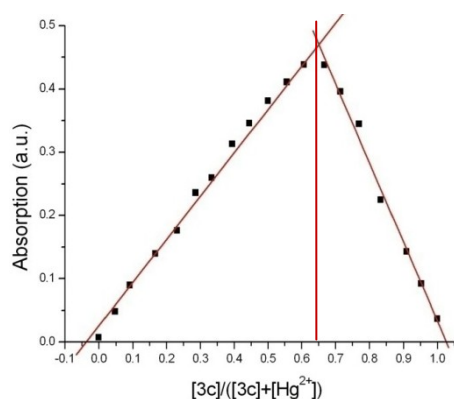
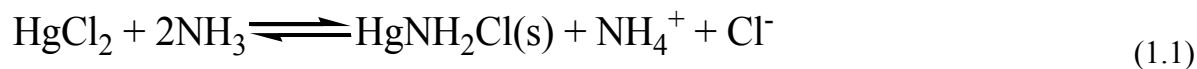


**Figure 6.** Invariant concentration Job plot of molecule **3c** to mercury in acetonitrile.

This 2:1 stoichiometry was unexpected and not desirable. The stoichiometry is different than most mercury/molecule complexes and thus, relative binding affinity cannot be compared between this complex and others in the literature. Moreover, as two molecules are required for each mercury ion, this stoichiometry consequentially requires more molecules to get a response than is ideal. It was wondered what the role of the second equivalent of the molecule was in the overall binding. Cotton et al. suggested a possible role. Specifically, it was noted that “This ligand (Ammonia) reacts in a unique way with mercury(II) compounds”<sup>19</sup>. As shown in equation 1.1,<sup>19</sup> one of the ammonia acted merely as a proton acceptor. Thus, despite of a seemly 2:1 ratio of reacted ammonia to mercury, the binding ratio between ammonia and mercury is actually 1:1.



This suggests to us that the 2:1 ratio initially observed in the invariant concentration Job plot could be “misleading” in terms of revealing the true binding ratio between mercury and molecule **3c**. To test this possibility, an invariant concentration Job plot in the presence of excess base was proposed, in the hope that such excess base would be more favorable as the proton acceptors, thus molecule **3c** would only be consumed as ligands to mercury complex. Table 3 shows the different base systems examined in sequence, and the reasoning for such selections. As can be observed, selection of base and ionic strength were important in obtaining a successful result.

**Table 3.** Different base systems for invariant concentration Job plot.

Base / Solvent	Result	Solution?
0.1M PhCOONa in acetonitrile	PhCOONa is not soluble in acetonitrile.	Find a more soluble base.
0.1M MeONa in MeOH	Yellow precipitates observed in mercury solution.	Find a weaker base.
Pure triethylamine	Yellow precipitates observed in mercury solution.	Try a lower base concentration.
10% (vol) triethylamine in acetonitrile	Yellow precipitates observed in mercury solution.	Try an even weaker base.
5% 0.1M pH = 7 phosphate buffer in acetonitrile	Salts just soluble enough at this concentration, yet water percentage is too high & no red-shift was observed.	Reduce buffer to sensor ratio from 20:1 to 4:1.
1% 0.1M pH = 7 phosphate buffer in acetonitrile	Job plot shows 1:1 binding ratio.	Not necessary.

Finally, a Job plot in 1% aqueous buffer and 99% acetonitrile solution avoided the consumption of molecule **3c** as a sacrificial proton acceptor, and revealed a 1:1 binding ratio between molecule **3c** and mercury complex, as shown in Figure 7. Under these conditions, a first order binding constant was then obtained. This result suggests a 4-member ring complex, as shown in Figure 8. Such 4-member ring mercury complexes have been reported earlier by Ancker, et al., and the structure of this mercury complex was characterized by X-ray diffraction, as shown in Figure 9.<sup>20</sup>

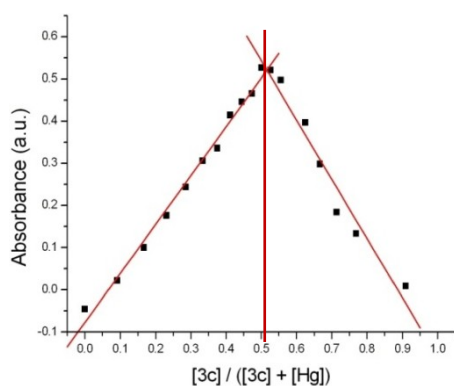


**Figure 7.** Invariant concentration Job plot of molecule **3c** to mercury in 1% aqueous buffer and 99% acetonitrile.

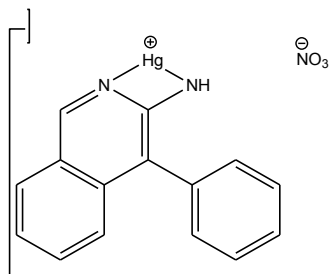


**Figure 8.** Suggested structure of the complex formed between molecule **3c** and mercury nitrate.

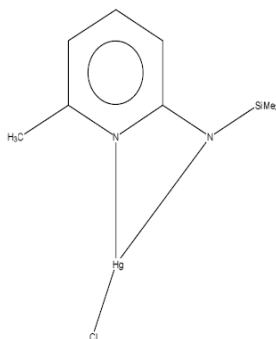


**Figure 9.** A similar mercury complex characterized by X-ray diffraction by Ancker, et al.<sup>20</sup>

A qualitative test of binding revealed a ~40nm red-shift in the UV absorption peak when molecule **3c** was exposed to mercury ion (Figure 10). To calculate the binding constant  $K_a$  from Benesi-Hildebrand plot, different concentrations of molecule **3c** were added to mercury solutions of much greater concentration (Figure 11). Under these conditions, it is considered that all molecule **3c** added to the solution was bound to excess mercury, which has no absorption at 400 nm. Thus, the observed peak in corresponding UV spectra at 400 nm, corresponds solely to the absorption of molecule/mercury complex. Figure 12 is the Benesi-Hildebrand plot constructed from these data, and a  $K_a$  of  $4.94 \times 10^4 \text{ M}^{-1}$  was calculated. While zinc ion is the only cation that exhibited a small new peak around 410 nm, corresponding to a  $K_a$  of  $7.49 \times 10^2 \text{ M}^{-1}$ , none of the other metal cations examined gave any change to the UV spectrum of molecule **3c** (Table 4). A detailed procedure for measuring the binding constant  $K_a$  from UV spectra is provided in the experimental section.

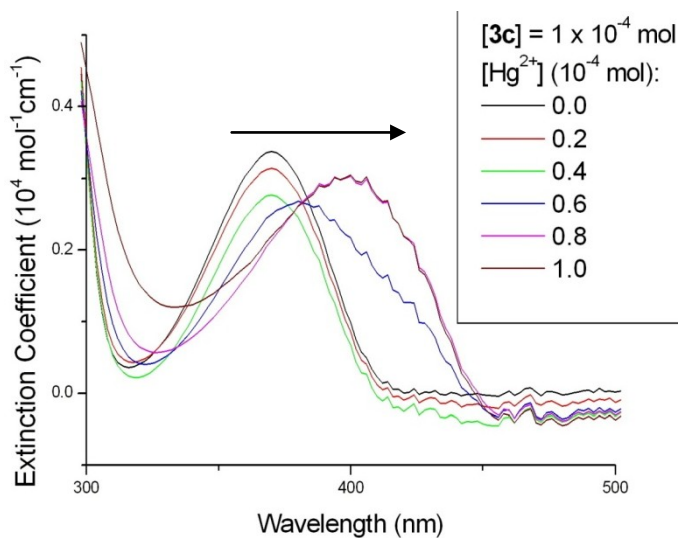


**Figure 10.** Binding of molecule **3c** to mercury shows an obvious red shift upon increasing mercury concentration, in 0.5% 0.1 M phosphate buffer and 99.5% acetonitrile.

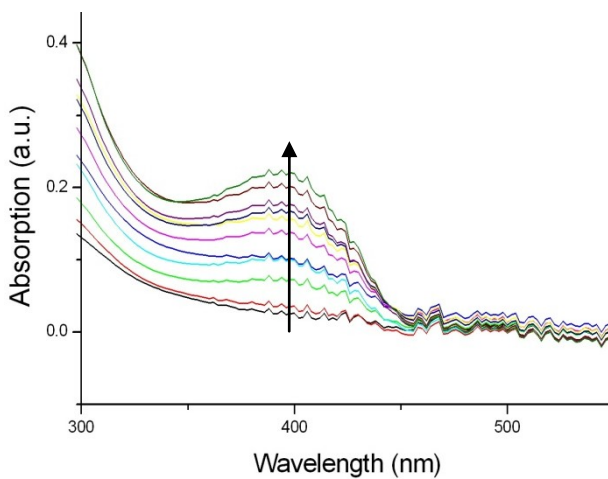


**Figure 11.** Addition of molecule **3c** to mercury solution, where the concentration of mercury solution stays at 1 mM, while the concentration of molecule **3c** solution varies from 0 to 50  $\mu\text{M}$ . Solvent: 2% 0.25 M phosphate buffer and 98% acetonitrile.

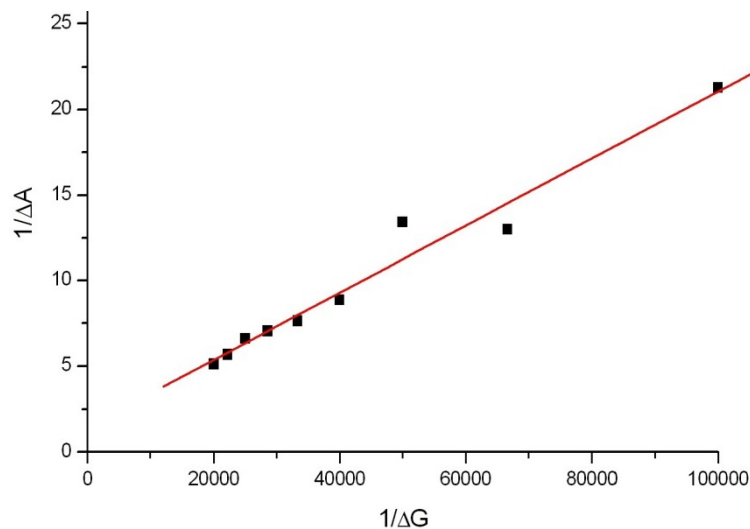


**Figure 12.** Benesi-Hildebrand plot reveals the binding constant between molecule **3c** and mercury:  $K_a = 4.94 \times 10^4 \text{ M}^{-1}$ .

**Table 4.** Binding constant  $K_a$  of molecule **3c** to different metal cations, calculated by Benesi-Hildebrand plot.

Metal Cation	Hg <sup>2+</sup>	Zn <sup>2+</sup>	Li <sup>+</sup> , Na <sup>+</sup> , K <sup>+</sup> , Ag <sup>+</sup> , Cd <sup>2+</sup> , Pb <sup>2+</sup> , Co <sup>2+</sup> , Ca <sup>2+</sup> , Sr <sup>2+</sup> , Ba <sup>2+</sup> , La <sup>3+</sup> , Tl <sup>3+</sup>
$K_a(\text{M}^{-1})$	$4.94 \times 10^4$	$7.49 \times 10^2$	Too small to measure by this method

However, the structure of molecule **3c** resembles that of the commercially available isoquinoline-3-amine. As shown in Figure 13, molecule **3c** has one more substituent benzene ring, which provides extra electron density. Such an increase in electron density was later proven to be crucial for the sensing of mercury ion: as shown in Figure 14, isoquinoline-3-amine did not respond to the same concentration of mercury ion, but molecule **3c** incurred an obvious peak at 400 nm, corresponding to a  $K_a$  of  $7.49 \times 10^2 \text{ M}^{-1}$ , as reported above in Figure 12 and Table 4.

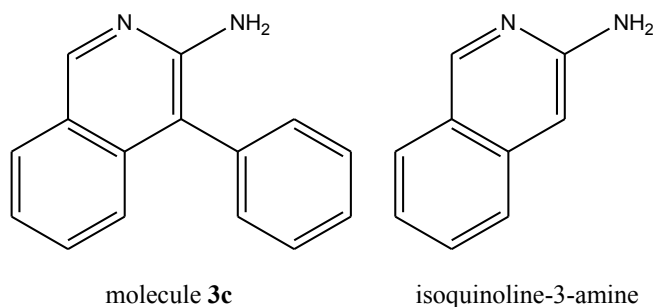


**Figure 13.** Structure comparison between molecule **3c** and isoquinoline-3-amine.

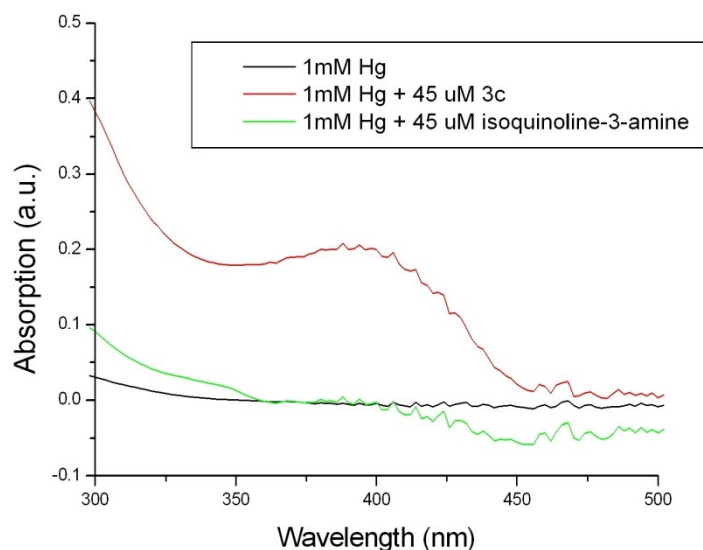


**Figure 14.** Binding constant comparison between molecule **3c** and isoquinoline-3-amine in 0.5% 0.1M phosphate buffer and 99.5% acetonitrile. Addition of molecule **3c** incurred an obvious peak at 400 nm, but the same concentration of isoquinoline-3-amine did not incur any peak at 400 nm.

The binding constant  $K_a$  of molecule **3c** to mercury ion could also be measured by Stern-Volmer plot. However, because oxygen is a much stronger fluorescence quencher than mercury, this method is not a convenient way to measure concentration / binding constant.

(Figure 15) shows that flushing oxygen for 15 seconds reduced more than half of the fluorescence from molecule **3c** solution. Thus, the whole procedure of obtaining Stern-Volmer plot, which involves exposure of molecule **3c** solution to air/oxygen for much longer than 15 seconds, would inevitably introduce a great error in the amount of quenched fluorescence by oxygen, and thus produce a much greater error in calculated binding constant  $K_a$ .

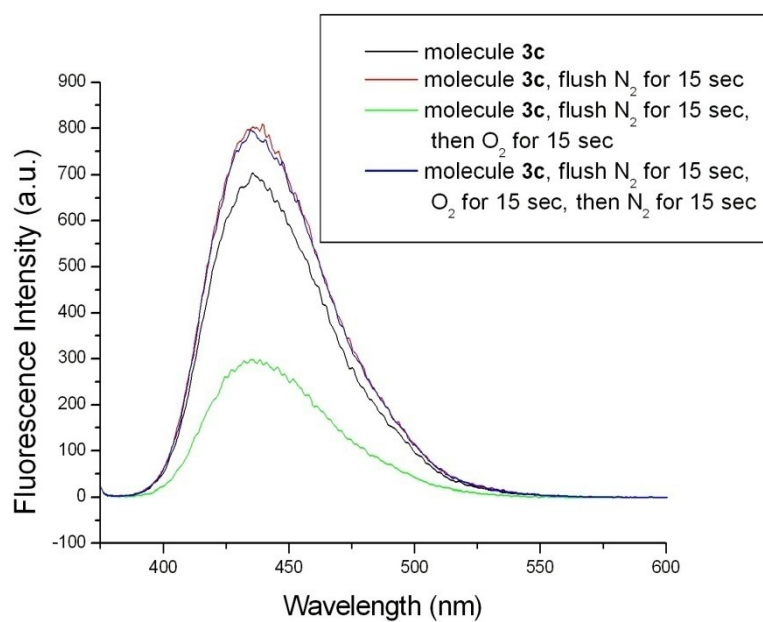


**Figure 15.** Oxygen dependent fluorescence quenching of molecule **3c**. Flushing oxygen for 15 seconds reduced more than half of the fluorescence of molecule **3c**, this quenching is reversible and the fluorescence of molecule **3c** can be recovered upon flushing nitrogen.

The lowest detection limit of molecule **3c** to mercury ion was found to be approximately 0.1 ppm (0.5  $\mu$ M) in both organic (acetonitrile) and aqueous (dimethylsulfoxide:water = 4:1) media. At this concentration, only a 3:1 ratio of signal to noise was measured. In mixed ion

sensing studies, where molecule **3c** and mercury ion were mixed with the same concentration of  $\text{Li}^+$ ,  $\text{Na}^+$ ,  $\text{K}^+$ ,  $\text{Ag}^+$ ,  $\text{Cd}^{2+}$ ,  $\text{Pb}^{2+}$ ,  $\text{Co}^{2+}$ ,  $\text{Ca}^{2+}$ ,  $\text{Sr}^{2+}$ ,  $\text{Ba}^{2+}$ ,  $\text{La}^{3+}$ , and  $\text{Tl}^{3+}$ , molecule **3c** displayed the same lowest detection limit, which further illustrated its high selectivity towards mercury ion.

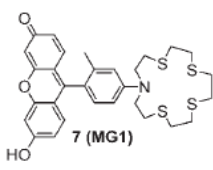
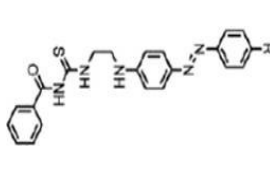
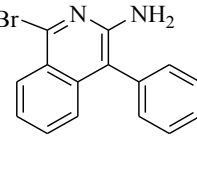
## 2.3 Conclusions

To date, four different molecules have been successfully synthesized as possible mercury sensors. The most promising mercury sensor among them was found to be molecule **3c**, which can be easily synthesized in grams (3 steps, 55% overall yield), yet has a very high fluorescence quantum yield ( $\Phi = 0.87$ ), high sensitivity and selectivity towards mercury ion in both organic and aqueous media. The binding constant of molecule **3c** was found to be  $4.94 \times 10^4 \text{ M}^{-1}$  to mercury, but only a maximum of  $7.49 \times 10^2 \text{ M}^{-1}$  to all other metal cations examined.

Molecule **3c** also showed considerable advantages over two of the most promising organic dye based sensors<sup>13,17</sup> reported in recent literature, as shown by the comparison given in Table 5. Among these sensors, molecule **3c** is much easier to synthesize with a much higher overall yield. Although binding constants of the other two molecules were not reported, the binding constant of molecule **3c** is comparable to or greater than any others reported. Molecule **3c** is also highly selective towards mercury ion, demonstrated by the mixed ion sensing experiment above; and its selectivity towards mercury ion can be measured by different methods (e.g. colorimetric, UV, and fluorescence). All these data

suggest that molecule **3c** is a very promising organic dye based mercury sensor.

**Table 5.** A quantitative comparison of molecule **3c** to other promising organic dye based mercury sensors.

<b>Sensor Molecule</b>				
<b>Reference</b>		13	17	This work ( <b>3c</b> )
<b>Synthesis</b>		4 steps, 5% overall yield	2 steps, 23-39% overall yield	3 steps, 55% overall yield
<b>Binding Constant <math>K_a</math></b>		NR*	NR*	$4.94 \times 10^4$
<b>Detection Method &amp; Limit</b>	<b>Colorimetric</b>	NR*	4 ppm (20 $\mu$ M)	20 ppm (100 $\mu$ M)
	<b>Fluorescence</b>	0.03 ppm (0.15 $\mu$ M)**	NR*	0.1 ppm (0.5 $\mu$ M)**

NR\* = Not reported

\*\* : Both detection limits are measured at signal/noise = 3/1 ratio.

Some preliminary results suggest possible routes for the continuation of this project. A series of molecules with fused aromatic rings were synthesized by this methodology, and could be modified in different ways to make potential sensors for different metal cations. For example, several thiophene molecules shown in Figure 16 were successfully synthesized and characterized by group member Weijun Niu. Their photophysical and binding properties to metal cations have yet to be examined.

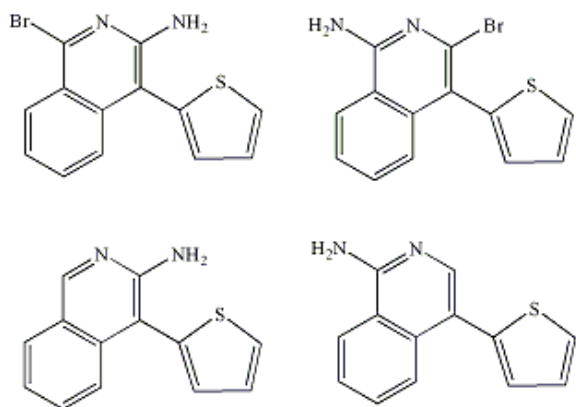


**Figure 16.** Available thiophene molecules for future examination.

Moreover, because the performance of molecule **3c** as a mercury sensor did not decrease in the presence of water as a potential competing reagent, a water soluble version of molecule **3c** is proposed in

Figure 17. Such structures employed the hydrophilic  $-\text{SO}_3\text{Na}$  group to increase the solubility of the whole sensor in aqueous medium, yet retained the crucial structure to mercury binding (the 2-aminopyridine function with high electron density). These proposed molecules could be synthesized and examined as potential aqueous mercury sensors. The fact that the mercury sensor itself is water soluble would allow a completely aqueous testing of mercury waste in aqueous systems; and a lot of other solvents can be tested, as the extinction coefficient of molecule **3c** was found to vary remarkably in different solvents.

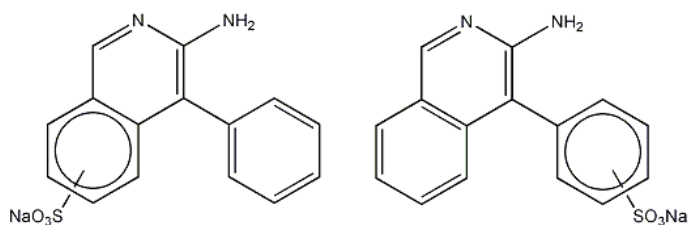


**Figure 17.** Proposed structures of water-soluble versions of molecule **3c**.

## 2.4 Experimental Section

### General Considerations

All chemicals were purchased from Aldrich or Acros. Acetonitrile was dried by distillation over  $\text{CaH}_2$ . Anhydrous dichloroethane in a sure seal bottle was purchased from Acros and used without further drying. Tetrabutylammonium hexafluorophosphate ( $\text{TBAPF}_6$ ) was recrystallized three times from ethanol. Mercury nitrate monohydrate was used as mercury source in all concerning measurements. All synthesis steps below were firstly examined and characterized by group member Weijun, Niu. The buffer concentrations were chosen at a minimum level (4:1 ratio) to both provide excess “proton acceptor” and minimize a decrease in the solubility of molecule **3c** in mixed solvent system.

**Synthesis of 3a.** To a flask containing 822.9 mg (7.4 mmol) of potassium tert-butoxide in 10 mL dimethylformamide (DMF), cooled in an ice bath, a mixture of 656.0 mg (4.8 mmol) 2-chlorobenzonitrile (**1**) and 430.4 mg (3.7 mmol) 2-phenylacetonitrile (**2**) in 6 mL DMF was added drop wise. The reaction mixture was then stirred at room temperature (RT) for 1 h, after which 20 mL saturated ammonium chloride (aq.) was added to quench excess potassium tert-butoxide. The resulting solution was extracted with ether, washed with

deionized water (DI), and dried over anhydrous sodium sulfate. Column purification with dichloromethane (DCM) and gradient addition of methanol, followed by removal of solvent and further drying under vacuum gave light yellow crystals (780.1 mg, 97% yield). Alternatively, this reaction was carried out on a larger scale (6.6 g, 71% yield) and the column purification step was replaced by recrystallization from hot ethanol.

**Synthesis of 3b.** To a flask containing 625.5 mg (2.9 mmol) of **3a**, 7 mL of 45% HBr in acetic acid was added. The resulting solution turned yellow and was stirred at RT for an additional 2 h. A 10 mL portion of ethyl acetate was added and, a yellow solid precipitated out. This solid was filtered and then washed with ether. This solid was re-dissolved in 40 mL of ethyl acetate, neutralized by saturated sodium hydrogen carbonate (aq.), and dried over anhydrous sodium sulfate. Column purification with DCM and gradient addition of methanol, followed by removal of solvent and further drying under vacuum gave yellow crystals (620.0 mg, 72% yield). Alternatively, this reaction was carried out on a larger scale (4.0 g, 60% yield) and the column purification step was replaced by recrystallization from hot ethanol. <sup>1</sup>H-NMR (CDCl<sub>3</sub>): 4.33 (s, 2H), 7.17-7.52 (9H), 8.05 (d, 1H).

**Synthesis of 3c.** To a Schlenk flask containing a mixture of 2.0 mL of 4N potassium hydroxide and 2.0 mL of methanol, 107.0 mg (0.4 mmol) of **3b** was added slowly under nitrogen protection. Then a mixture of 60.0 mg (0.03 mmol) of 5% Pd on activated carbon and 60.0 mg (1.6 mmol) of sodium borohydride was added, and the mixture was stirred at RT overnight. The resulting mixture was washed with tetrahydrofuran (THF) and dried over anhydrous sodium sulfate. Column purification with DCM and gradient addition of methanol, followed by removal of solvent and further drying under vacuum gave a light yellow solid

(741.0mg, 79% yield). <sup>1</sup>H-NMR (DMSO): 3.25 (s, 1H), 5.19 (s, 1H), 7.01 (d, 1H), 7.12 (t, 1H), 7.24 (t, 1H), 7.27 (t, 1H), 7.33-7.52 (4H), 7.80 (d, 1H), 8.82 (s, 1H). MS: 221 (in acidic solution).

**Synthesis of 5a.** To a Schlenk flask containing a mixture of 768.3 mg (5.6 mmol) of 2-chloro-benzonitrile (**1**), 1.2063 g (8.4 mmol) of 2-cyanophenyl acetonitrile (**4**), and 1.9391 g (17.3 mmol) of potassium tert-butoxide, 12 mL of anhydrous THF was added through a syringe. The reaction mixture was stirred under reflux in an oil bath for 18 h, and then 30 mL of saturated ammonium chloride (aq.) was added to quench excess potassium tert-butoxide. The resulting solution was extracted with DCM and dried over anhydrous sodium sulfate. Column purification with DCM and gradient addition of methanol, followed by removal of solvent and further drying under vacuum gave a red solid (990.0 mg, 73% yield).

**Synthesis of 5b.** To a flask containing 434.7 mg (1.8 mmol) of **5a**, a mixture of 10 mL of 45% HBr in acetic acid and 10 mL of DCM was added, and stirred at RT overnight. A portion of 100 mL ether was added and, a yellow solid was precipitated and filtered. Then this solid was re-dissolved in 50 mL of THF, neutralized by saturated sodium hydrogen carbonate (aq.), and then dried over anhydrous sodium sulfate. Column purification with DCM and gradient addition of methanol, followed by removal of solvent and further drying under vacuum gave a light yellow solid (341.1 mg, 59% yield). <sup>1</sup>H-NMR (DMSO): 4.60 (br, 2H), 7.89-8.93 (8H).

**Synthesis of 5c.** To a Schlenk flask containing a mixture of 2.0 mL of 4N potassium hydroxide and 2.0 mL of methanol, 76.0 mg (0.2 mmol) of **5b** in 0.96 mL of THF was added slowly under nitrogen protection. Then a mixture of 48.0 mg (0.04 mmol) of 5% Pd on

activated carbon and 90.0 mg (2.4 mmol) of sodium borohydride was added, and stirred at RT for 3 days. The resulting mixture was washed with THF and dried over anhydrous sodium sulfate. Column purification with DCM and gradient addition of methanol, followed by removal of solvent and further drying under vacuum gave a light yellow solid (439.0mg, 76% yield). <sup>1</sup>H-NMR (CDCl<sub>3</sub>): 3.50 (br, 2H), 7.44-7.80 (6H), 8.04 (t, 1H), 8.82 (t, 1H), 9.28 (s, 1H). MS: 246 (in acidic solution).

**Procedure for obtaining electronic absorption spectra.** Solutions of 0.2 mM **3b**, **3c**, **5b**, and **5c** in acetonitrile were prepared. A UV cuvette of 1 cm path length, filled with acetonitrile, was measured as a blank. Then each of the prepared solutions were measured using a HP 8452A UV/Vis spectrophotometer. Extinction coefficients were calculated by Beer's Law:  $\epsilon = A/bc$ , where  $\epsilon$  is the extinction coefficient, A is the measured absorbance, b is the length of cuvette (1 cm), and c is the concentration of standard solutions (0.2 mM). These data were plotted as extinction coefficient versus wave length in Microcal Origin 6.0.

**Procedure for measuring quantum yield.** Standard solutions of 25  $\mu$ M **3b**, **3c**, **5b**, **5c**, and 2-Aminopyridine (standard) in acetonitrile were prepared in dry box. A fluorescence cuvette of 1 cm path length, filled with acetonitrile, was measured as a blank. Then a series of solutions containing 3.0 mL standard solution, 2.5 mL standard solution + 0.5 mL acetonitrile, 2.0 mL standard solution + 1.0 mL acetonitrile, 1.5 mL standard solution + 1.5 mL acetonitrile, 1.0 mL standard solution + 2.0 mL acetonitrile, and 0.5 mL standard solution + 2.5 mL acetonitrile, respectively, were prepared individually, taken out of dry box in a sealed fluorescence cuvette, and measured fluorescence signal from 375 to 600 nm (excited at 370 nm, slit = 4.0 nm). The recorded data were graphed in Microcal Origin 6.0. The area

under each curve was integrated, and the integrated area under the blank curve was subtracted from all other sample curves. A plot of subtracted fluorescence area versus absorbance was generated, and quantum yields of **3b**, **3c**, **5b**, and **5c** were calculated by comparing their slopes to the slope of the standard, 2-Aminopyridine ( $\Phi = 0.87$ ), as the quantum yields are proportional to the slopes in a plot of integrated fluorescence area versus absorbance.

**Procedure for measuring binding constant  $K_a$  from UV spectra.** Stock solutions of 2 mM mercury nitrate and 0.1 mM molecule **3c** were prepared in mixed solvent of 98% acetonitrile and 2% 0.25 M aqueous phosphate buffer. A UV cuvette of 1 cm path length, filled with the mixed solvent, was measured as a blank, then a series of solutions each containing 1 mL stock solution of mercury nitrate, 0, 0.1, 0.2, ..., 1.0 mL stock solution of molecule **3c**, and 1.0, 0.9, ..., 0.1, 0 mL mixed solvent, were prepared and measured absorbance immediately. These data were plotted as absorption versus wave length in Microcal Origin 6.0. At the peak wavelength, the differences in absorbance and the differences in molecule **3c** concentration were plotted as  $1/\Delta A \sim 1/\Delta[3c]$ , and the binding constant  $K_a$  was calculated by the equations below:

$$\Delta\varepsilon = \frac{1}{b \times C_0 \times \text{intercept}} \quad (2.1)$$

$$K_a = \frac{1}{b \times C_0 \times \text{slope} \times \Delta\varepsilon} \quad (2.2)$$

where  $\Delta\epsilon$  is the difference in extinction coefficient,  $b$  is the path length of the cuvette (1 cm),  $C_0$  is the concentration of mercury nitrate, and intercept and slope are calculated from the linear fit of the plot.

**Procedure for measuring binding ratio from Job plot.** Standard solutions of 0.25 mM molecule **3c** and 0.25 mM  $\text{Hg}^{2+}$  in acetonitrile were prepared in acetonitrile or a mixed solvent of 99% acetonitrile and 1% 0.2 M aqueous phosphate buffer. A series of solutions with different ratios of **3c**: $\text{Hg}^{2+}$  (range from 1:20 to 20:1) were prepared and measured absorbance immediately. Then different absorbances were plotted versus the mole fraction of molecule **3c**:  $[3c] / ([3c] + [\text{Hg}^{2+}])$ . This plot is called Invariant Concentration Job plot, and the solution composition at the peak corresponds to the binding ratio of molecule **3c** to mercury ion.

## Chapter 3

---

### **MOLECULAR TRANSISTOR PROJECT**

### 3.1 Introduction

Since Richard Feynman proposed the trend of “getting smaller and smaller” in his talk “There’s Plenty of Room at the Bottom” at the annual meeting of the American Physical Society in 1959,<sup>21</sup> there has been numerous attempts to build smaller and smaller electronics for the application in both research and industry, because smaller sized electronics allows higher circuit density and faster processing speed. However, the traditional top-down, lithographic approach is reaching its limit in smallest achievable feature size;<sup>22</sup> and further reduction in feature size may benefit from a new method – the bottom-up approach of molecular-based self-assembly. Despite of the cost advantage and convenience of synthesis that the bottom-up molecular-based self-assembly approach offers, there are considerable challenges as well. Two of the most obvious challenges are: how to bridge molecular scale (~1 nm) and lithographic scale (~100 nm), and how to ensure the correct orientation of inserted molecules.

In this project, orthogonal self-assembly of a molecule between two nanoparticles was employed to attempt to solve these two problems. First of all, orthogonal self-assembly ensures the correct orientation of inserted molecules because different ending groups bind preferentially to different particles. Then, upon linking two particles of 10 - 20 nm in diameter together, the resulting structure can plausibly be inserted into features defined on a surface using lithography techniques. The general scheme behind this idea is shown in Figure 18 and is explained as follows.

A molecule is usually 1 - 2 nm in length, while the lower limit of defined lithographic scale is 20 - 50 nm. Synthesizing 2 nanoparticles of 10 - 20 nm diameter each, then linking

them together with a linker molecule will create a structure of approximately 20 - 40 nm in size. Such structures are defined as shown in Figure 18: two identical nanoparticles linked together by a two-end linker is defined as a homo-dimer, while two different nanoparticles linked together by a two-end linker is defined as a hetero-dimer. In the same fashion, three identical nanoparticles linked together by a three-end linker is defined as a homo-trimer, while two identical and one different nanoparticles linked together by a three-end linker is defined as a hetero-trimer.



**Figure 18.** A cartoon of the definition of (from left to right) homo-dimer, hetero-dimer, homo-trimer, and hetero-trimer.

Orthogonal Self-Assembly was firstly proposed by Wrighton and Whitesides in their 1989 Science paper as “In formation of Self-Assembly Monolayers (SAMs), (absorbant)  $A_i$  adsorbs strongly on (surface)  $S_i$  but weakly on  $S_j$ , while  $A_j$  adsorbs strongly on  $S_j$  but weakly on  $S_i$ ”. This paper was also the first to demonstrate the preferential binding of disulfide onto gold surface, and carboxylic acid onto alumina surface by the appearance of new XPS peaks corresponding to sulfur on gold only and oxygen (from carboxylic acid) on alumina only.<sup>23</sup> Later on, Wrighton and Whitesides also demonstrated the preferential binding of isocyanide onto platinum surface by the same method.<sup>24</sup>

However, our group discovered that such binding preferences to surface do not

necessarily apply to nanoparticles.<sup>25</sup> This study was done primarily by monitoring the IR spectra of different incubated samples, as bound and unbound thiol and isocyanide display peaks at different positions in IR spectra. The linker molecule synthesized in this paper has two different ends – thiol and isocyanide, thus showing a peak around 1710  $\text{cm}^{-1}$  for thiol, and a peak around 2120  $\text{cm}^{-1}$  for isocyanide. When incubated with gold particles, the 1710  $\text{cm}^{-1}$  peak shifted, while the 2120  $\text{cm}^{-1}$  peak remained unchanged, suggesting that only the thiol end of the linker bound to gold particles. However, when incubated with platinum particles, both 1710  $\text{cm}^{-1}$  peak and 2120  $\text{cm}^{-1}$  peak shifted, suggesting that both the thiol end and the isocyanide end of the linker bound to platinum particles. Furthermore, in a competing experiment, when this linker molecule with both thiol and isocyanide ends were incubated with platinum substrate, the IR spectrum showed a large 2120  $\text{cm}^{-1}$  peak corresponding to unbounded isocyanide, versus a very small 2158  $\text{cm}^{-1}$  peak corresponding to bounded isocyanide, further suggesting that the binding preference of isocyanide to platinum previously concluded by Wrighton and Whitesides<sup>24</sup> is only valid when the competition of thiol is excluded. These results indicated a new dimension when thinking about orthogonal self-assembly in the case of nanoparticles, and binding preference of carboxylic acid to metal oxide nanoparticles should also be examined, as a continuation of this project.

To complete this project, phenylethynyl oligomer (OPE) linker molecules with different ending groups were synthesized. OPEs were chosen because they are rigid and thus of well-defined end-to-end length. Moreover, they are preceded “molecular wire” candidates,<sup>26,27</sup> and thus reasonable as part of a conducting pathway. It was envisioned to synthesize metal and metal oxide nanoparticles using literature procedures with small

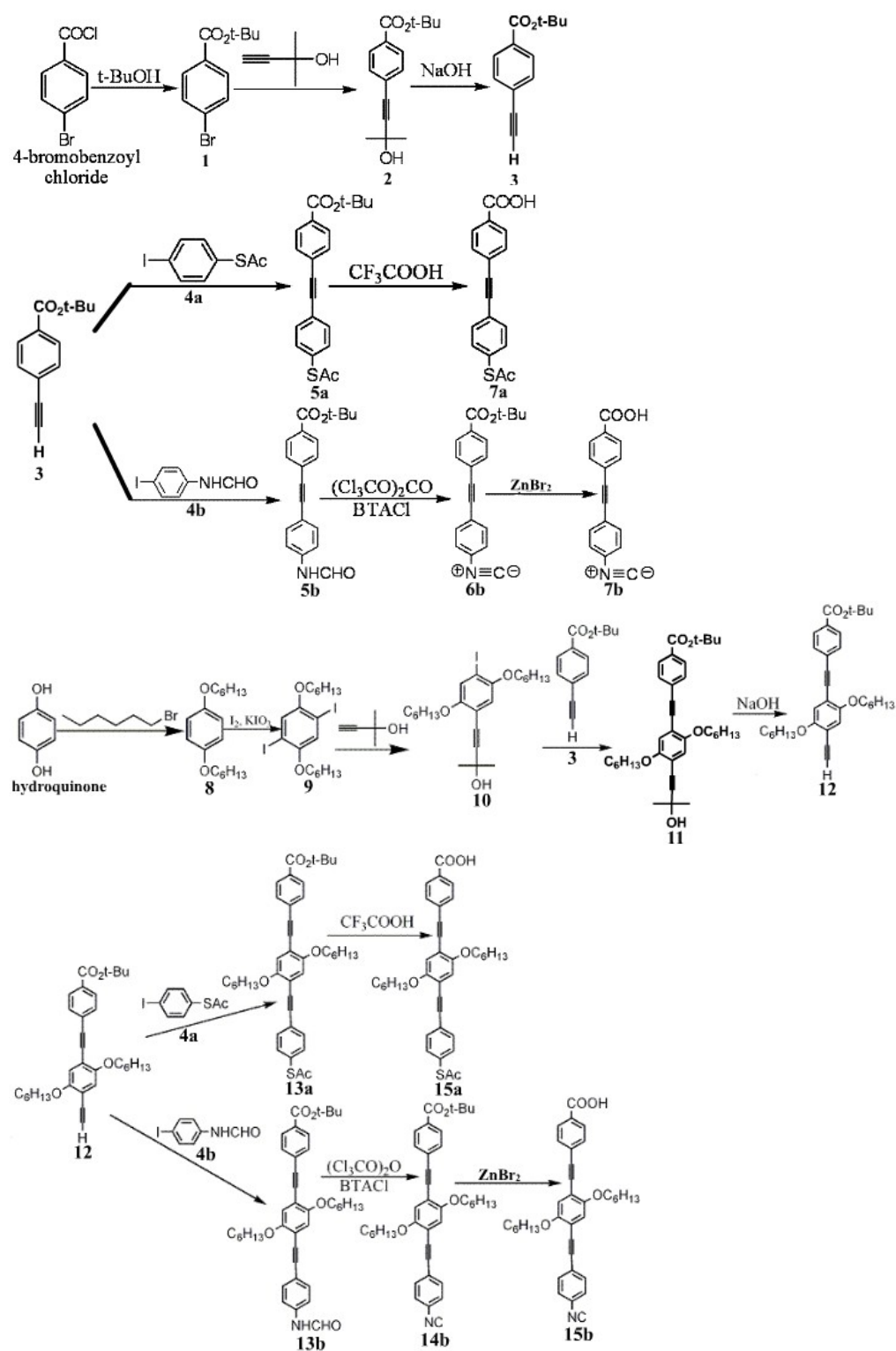
modifications. As will be discussed in detail below, some of these modifications were not completely straightforward, and some fundamental questions about ideal conditions for nanoparticle preparation still exist. It is then planned to synthesize a series of homo- and hetero- dimers and trimers with the self-assembly technique, and to examine their properties in different ways.

## 3.2 Results and Discussion

### 3.21 Synthesis and Characterization of Linker Molecules

Synthetic routes for all four target linker molecules are shown in Scheme 3. The OPE linkage was chosen for reasons discussed above. The thiol, isocyanide and carboxylic ending groups were chosen to bind preferentially to gold, platinum, and metal oxide nanoparticles accordingly, as explained in the above mentioned literature reports. There were several challenges in the actual synthesis, but they were all addressed properly by judicious alteration of reactions reported in the literature. For example, the previously reported, low-yield (~30%) method<sup>28</sup> for the synthesis of molecule 4a used previously in the group, was replaced by a new, higher-yield method.<sup>29</sup> The low solubility of 3-ring linkers was improved by adding side chains (-OC<sub>6</sub>H<sub>13</sub>) to the middle ring. And the hydrolysis of isocyanide group during the deprotection of *tert*-butyl group, was solved by employing a mild reagent - zinc bromide.<sup>30</sup> Full details of every synthetic step are provided in the experimental section.

**Scheme 3.** Synthetic routes to four target linker molecules.



### 3.22 Synthesis of Metal and Metal Oxide Nanoparticles

Water-soluble gold nanoparticles have been widely reported and are commercially available.<sup>31</sup> Moreover, synthesis of both water-soluble and organic-soluble platinum nanoparticles has been reported.<sup>32</sup> On the other hand, metal oxide nanoparticles are much less studied. The most mono-dispersed metal oxide nanoparticles reported recently are oleic acid capped, organic-soluble iron oxide nanoparticles synthesized by Hyeon, et al.<sup>33</sup> The sizes of these nanoparticles could be controlled between 4 and 16 nm by controlling the ratio of iron source to ligand. We were able to reproduce these reported results and made mono-dispersed iron oxide nanoparticles of 7 nm diameter (Figure 19).

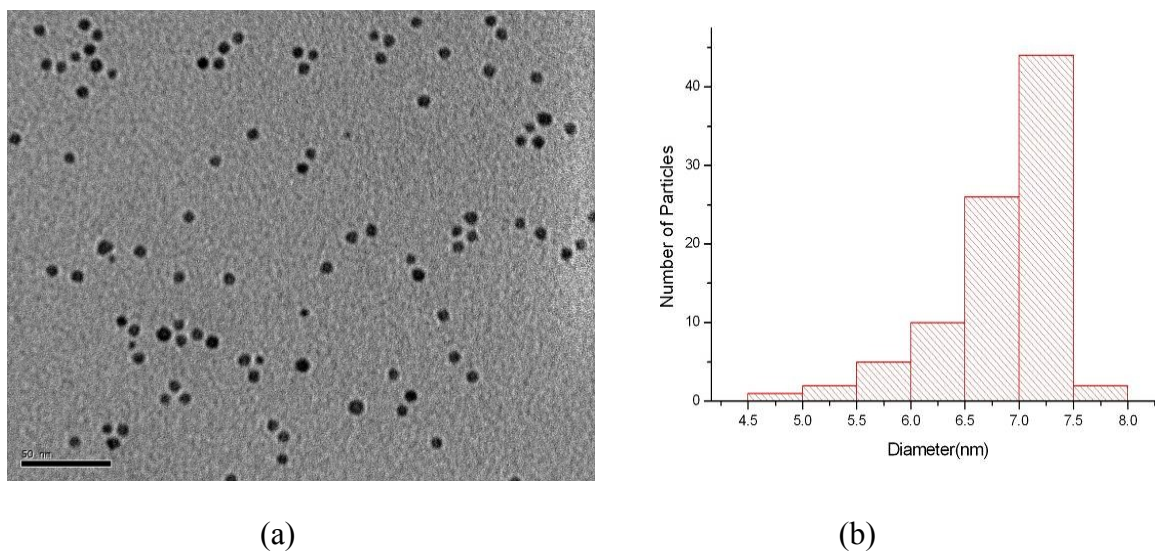


**Figure 19.** a) TEM image of 7 nm iron oxide nanoparticles; b) Histogram of the size distribution of nanoparticles in a).

### 3.23 Ligand Exchange Experiments

Since the metal nanoparticles and metal oxide nanoparticles were prepared in two

different, immiscible solvents, it was necessary to alter the solubility of one of them so that they could be combined in the same phase. This change could be accomplished by ligand exchange of the oleic acid groups on the iron oxide nanoparticles for shorter, water solubilizing ligands. A shorter ligand was preferred because the linker molecule must protrude from this ligand shell and the shortest ligands minimize the length required for the linker molecule. Longer linker molecules require more effort to synthesize and purify. It was appreciated, however, that the ligands exchanged onto the iron oxide nanoparticles still had to act to cap them and prevent their aggregation and subsequent agglomeration (e.g. fusing together).

A number of possible ligands were surveyed. These included formic acid, benzoic acid, citric acid, salicylic acid, succinic acid, tartaric acid, and glycerol. A mixture of oleic acid capped iron oxide nanoparticles dissolved in toluene and the salt of a potential ligand dissolved in deionized water were mixed and sonicated for 1 h, then allowed to stay at room temperature for additional 24 h for the completion of any possible ligand exchange. The vials with citric acid and tartaric acid showed a light brown color in the aqueous layer, while the vials with succinic acid and glycerol showed a light yellow color in the aqueous layer after ligand exchange. These layers were then individually removed using a pipette, and centrifuged with membrane in the hope that particles would be caught in the membrane, while excess ligands would filter through with solvent. The residues on the membrane were then collected and re-dissolved into DI for TEM analysis. Despite these promising increases in color in the aqueous layer, the ligand-exchanged products were not deemed to be suitable after TEM analysis. Figure 20 shows typical results from TEM analysis. In the left panel of

Figure 20, an aggregate of nanoparticles is shown. Most of the roughly spherical particles observed by TEM were aggregated after these ligand exchanges. In addition, other non-spherical objects were observed in the right panel of Figure 20. This debris may be dirt or impurities introduced by the ligand exchange process, or aggregation of excess ligand that were not removed upon purification, but in any event is not the desired result: dispersed, spherical nanoparticles.

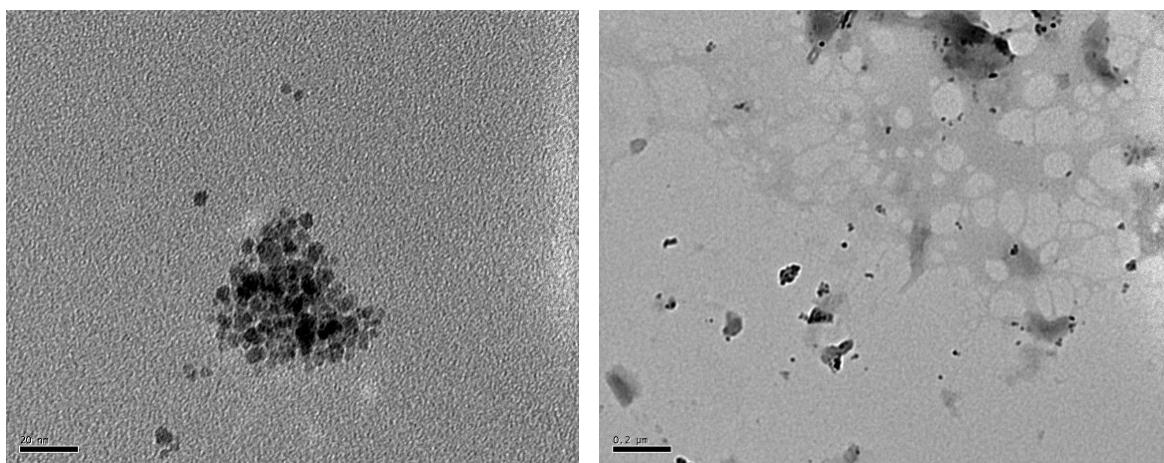
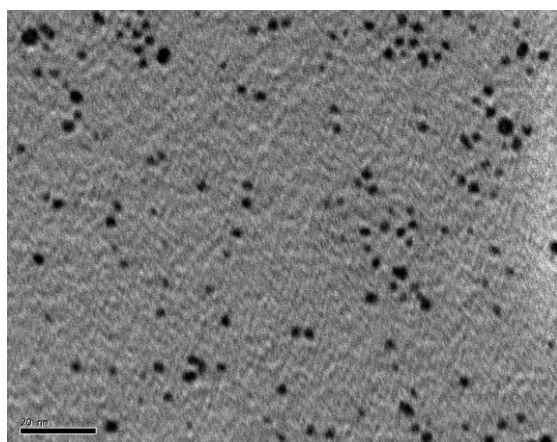


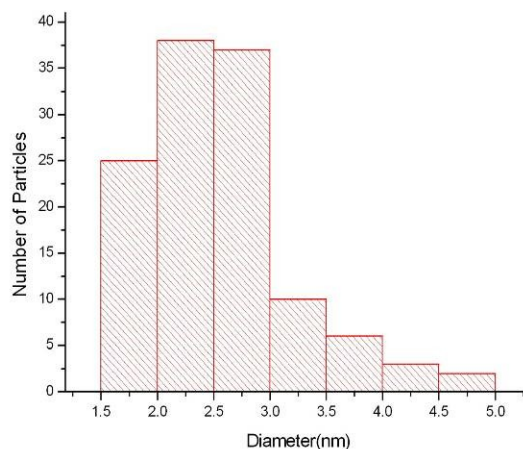
**Figure 20.** TEM images of iron oxide nanoparticle samples after ligand exchange with tartaric acid, showing (left) aggregated particles and (right) debris thought to result from aggregates of excess ligand that were not removed upon purification.

To avoid this problem, it was decided to follow literature procedures<sup>32,34</sup> on direct synthesis of hexanethiol capped, organic soluble gold and platinum nanoparticles. Toluene dispersions of both gold and platinum nanoparticles were prepared as described fully in the experimental section. TEM analysis of gold particles is shown in Figure 21a. A histogram of the size distribution (Figure 21b) shows that most particles are between 2 and 3 nm in size, which is a reasonable size distribution for subsequent experiments. TEM analysis of platinum

particles is shown in Figure 21c. A histogram of the size distribution (Figure 21d) shows that most particles are between 2 and 3 nm in size, which is also a reasonable size distribution for subsequent experiments.



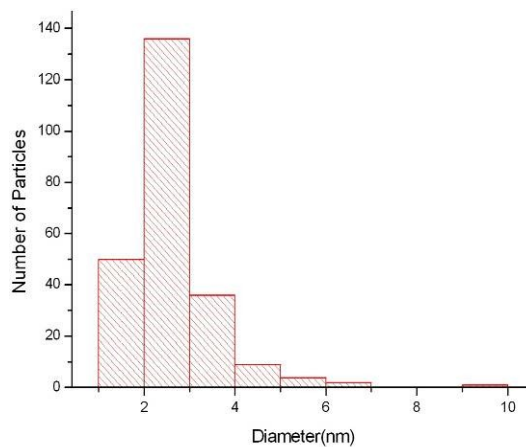
(a)



(b)



(c)



(d)

**Figure 21.** a) TEM image of 3nm gold nanoparticles capped by hexanethiol; b) Histogram of the size distribution of nanoparticles in a); c) TEM image of 3nm platinum nanoparticles capped by hexanethiol; d) Histogram of the size distribution of nanoparticles in c).

Thus, to date we have investigated and abandoned particle dimerization in aqueous solutions. This decision was made because no suitable route was found to prepare the iron-oxide particles in water, nor to apply ligand exchange on these particles to render them water soluble yet still retain their original size and shape. All three types of nanoparticles (iron oxide, gold and platinum) have, however, been prepared in organic solvents.

### **3.3 Conclusion**

The primary focus of the work reported in this chapter was to identify routes to particles with well defined, relatively mono-dispersed sizes and shapes. To date, we have successfully synthesized organic soluble iron oxide nano-particles, and both water and organic soluble gold and platinum particles of mono-dispersed sizes and shapes. Given that all particles have been synthesized in organic phase, it is possible now to consider binding them together.

### **3.4 Prospects for Synthesis of Nanoparticle Hetero-dimers and Hetero-trimers**

The next logical step in this work would be to dimerize the two different kinds of particles with the bifunctional ligands that were prepared. However, no specific attention was yet given as to whether the relative lengths of the capping ligands on the particles and the linker molecule were appropriate for dimerization (or trimerization with Y-shaped molecules synthesized by other group members). If a linker molecule is too short relative to the lengths of the capping ligand, it cannot span the two coatings around the particles and

bind them together. Thus, some simple geometry calculations were performed and presented here to assess the suitability of the particles and linker molecules currently in hand.

In order to link two nanoparticles into a hetero-dimer, the length of the linker must exceed the total length of both capping ligands on the particles so that the linker would be able to “get through” both layers of ligands and bind to both nanoparticles. As shown in Figure 22, we have gold nanoparticles with a 3 nm average diameter (1.5 nm average radius) that are capped with hexanethiol groups. The thickness of the hexanethiol capping ligand layer is estimated to be 0.9 nm from the minimum energy structure calculation in Chem 3D. We also have iron oxide nanoparticles with a 7 nm average diameter (3.5 nm average radius) that are capped with oleic acid groups. The thickness of the oleic acid capping ligand layer is estimated to be 1.66 nm from the minimum energy structure calculation in Chem 3D. To “get through” both hexanethiol ligand layer and oleic acid ligand layer, the theoretical minimum linker length is calculated to be  $0.9 \text{ nm} + 1.66 \text{ nm} = 2.56 \text{ nm}$ . However, the two-end linker molecules synthesized above are only 1.66 nm (molecule 7a and 7b) and 2.47 nm (molecule 15a and 15b) in length, respectively, calculated from the minimum energy structure calculation in Chem 3D. These calculations suggest that we have to either replace the long oleic acid capping ligand by some other shorter, organic-soluble capping ligand, or synthesize new linker molecules of longer length. Given the time-consuming nature of linker synthesis, and the general trend that longer linker molecules are less stable, the possibility of replacing the long oleic acid capping ligand by a shorter ligand is more attractive and will be examined next.

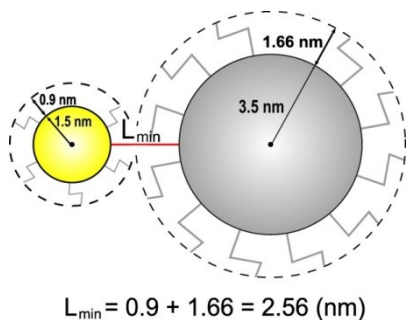
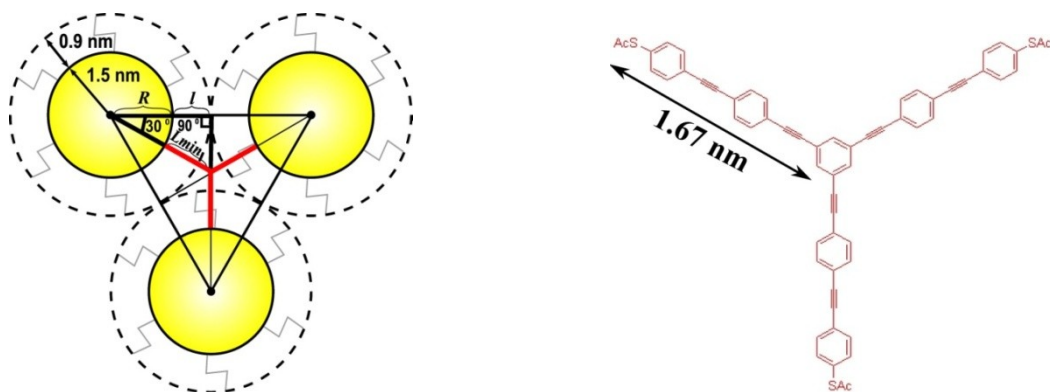


**Figure 22.** Minimum linker length calculation for gold-iron oxide hetero-dimer.

In a similar fashion, a simple geometry calculation on the homo-trimer raises the question as to whether the Y-shaped molecules available to us are long enough to prepare homo-trimers. This calculation was done as shown in Figure 23a. We have the same gold nanoparticles with a 1.5 nm average radius (“R” in Figure 23a) that are capped with a 0.9 nm layer of hexanethiol groups (“*l*” in Figure 23a). The minimum linker length (“ $L_{\min}$ ” in Figure 23a) is determined when 3 nanoparticles (including their hexanethiol layers) are tangent to each other. The angle between each 2 arms of the three-arm linker is a fixed value of  $120^\circ$ , defined by the rigid planar structure of the central benzene ring. Equation 3.1 shows the calculation of  $L_{\min}$  in the bold triangle in Figure 23a. The value of  $L_{\min}$  is calculated to be 1.27 nm. Group member Kusum Chandra has successfully synthesized the three-arm homo-linker as shown in Figure 23b, and the length on each arm of this linker is calculated to be 1.67 nm from the minimum energy structure calculation in Chem 3D, which could theoretically get through both layers of ligands. Thus, no further ligand exchange or linker synthesis is required for the self-assembly of the homo-trimer.



(a) Minimum linker length calculation

(b) Structure of 3-arm homo-linker

**Figure 23.** (a) The minimum linker length calculation for gold homo-trimer; (b) Structure and length of available three-arm homo-linker.

$$\sin 60^{\circ} = \frac{R+l}{R+L_{min}} \Rightarrow \frac{\sqrt{3}}{2} = \frac{1.5+0.9}{1.5+L_{min}} \Rightarrow L_{min} = 1.27 (nm) \quad (3.1)$$

In a similar fashion, a simple geometry calculation was performed for the minimum length of a molecule needed to bridge two gold nanoparticles with 1.5 nm radius and an iron oxide nanoparticle with a 3.5 nm radius. This calculation was performed as shown in Figure 24a. We have the same gold nanoparticles with a 1.5 nm average radius (“ $r_1$ ” in Figure 24a) that are capped with a 0.9 nm layer of hexanethiol groups (“ $l_1$ ” in Figure 24a), and iron oxide nanoparticles with a 3.5 nm average radius (“ $r_2$ ” in Figure 24a) that are capped with a 1.66 nm layer of oleic acid groups (“ $l_2$ ” in Figure 24a). The minimum linker length (“ $L_{min}$ ” in Figure 24a) occurs when 2 gold nanoparticles (including their hexanethiol layers) are tangent to the iron oxide nanoparticle (including its oleic acid layer). The angle between each 2 arms of the three-arm linker is a fixed value of  $120^{\circ}$ , defined by the rigid planar structure of

the central benzene ring. Equations 4.1 – 4.3 shows the calculation of  $L_{\min}$  in bold triangles in Figure 24a, and  $L_{\min}$  is calculated to be 1.95 nm. The synthesis of this three-arm hetero-linker (Figure 24b) was still in process by other group members. The length on the hetero-arm with carboxylic acid ending group is calculated to be 2.26 nm from the minimum energy structure calculation in Chem 3D, which is considerably larger than the theoretical minimum length. Thus, no further ligand exchange or linker synthesis is required for the self-assembly of the hetero-trimer.

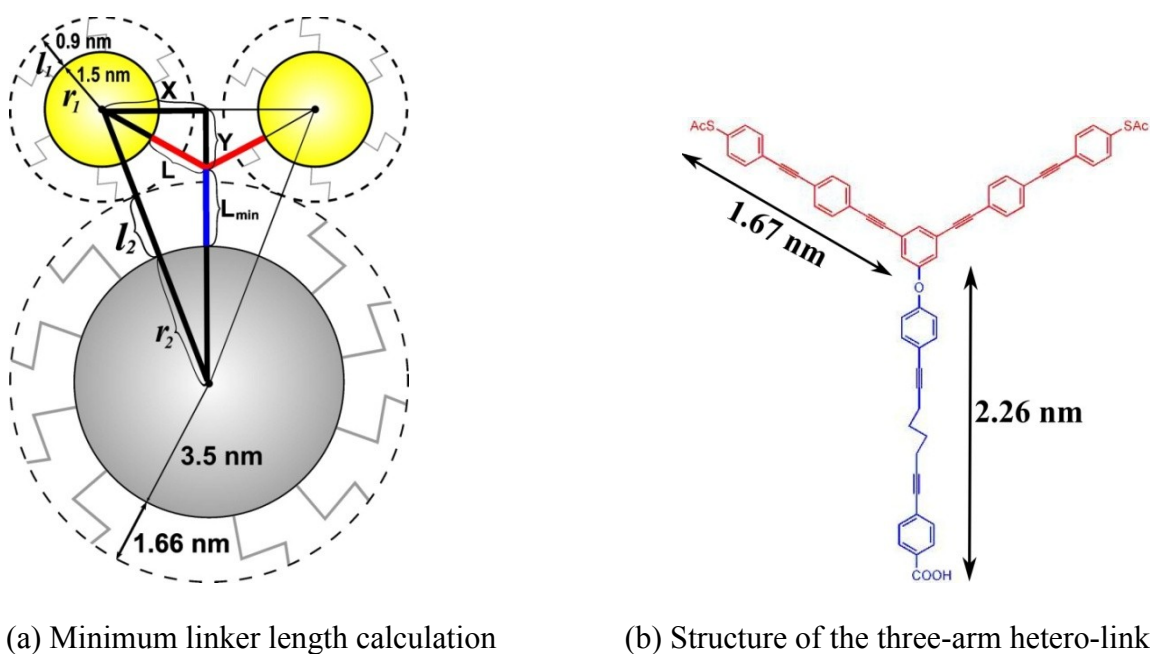


**Figure 24.** (a) The minimum linker length calculation for gold-iron oxide hetero-trimer; (b) Structure and lengths of the proposed three-arm hetero-linker.

$$X = (r_1 + L) * \sin 60^\circ = (1.5 + 1.67) * \frac{\sqrt{3}}{2} = 2.75 \text{ (nm)} \quad (4.1)$$

$$Y = (r_1 + L) * \cos 60^\circ = (1.5 + 1.67) * \frac{1}{2} = 1.59 \text{ (nm)} \quad (4.2)$$

$$L_{min} = \sqrt{(r_1 + l_1 + l_2 + r_2)^2 - X^2} - Y - r_2 = \sqrt{(1.5 + 0.9 + 1.66 + 3.5)^2 - 2.75^2} - 1.59 - 3.5 = 1.95 \text{ (nm)} \quad (4.3)$$

A summary of minimum linker lengths versus available linker lengths are shown in Table 6. As stated above, for both homo- and hetero-trimer, the linkers are longer than that required geometrically and thus should be suitable for self-assembly experiments. However, the available linkers for hetero-dimers are too short, because the oleic acid capping ligand on iron-oxide nanoparticles is too long.

**Table 6.** Minimum linker lengths by calculation versus available linker lengths.

	<b>Hetero-dimer</b>	<b>Homo-trimer</b>	<b>Hetero-trimer</b>
<b>Minimum Linker Length</b>	2.56 nm	1.27 nm	1.95 nm
<b>Available Linker Length</b>	1.66 nm 2.47 nm	1.67 nm	2.26 nm
<b>Future Alternation</b>	Ligand Exchange on Iron Oxide Nanoparticles	Not Required	Not Required

Thus, a continuation of this project would be ligand exchange on the oleic acid capped iron-oxide nanoparticles for a smaller but still organic soluble ligand. The exchange kinetics of this process have not been explored. Moreover, there are few established methods to

characterize the process of ligand exchange. Murray, et al. assessed the degree of ligand exchange on small (1 - 2 nm) gold nanoparticles by oxidizing the gold, collecting the organic ligands dissociated during this process and measuring the relative amounts of original and exchanged ligand.<sup>35</sup> This process is not convenient and, more importantly, it is not likely to be very accurate as the weight fraction of the particle to ligands increases. To be useful for TEM analysis and molecular electronics measurements, we have chosen particles that are much larger than the ones studied by Murray, et al.

Replacing the long oleic acid capping ligand by a shorter ligand appears to be most promising. However, we have admitted that the exchange process on iron-oxide nanoparticles is not yet characterized and thus there is no guarantee that it will work. Access to other types of metal oxide particles as backup options for synthesis and ligand exchange is thus desirable. Fortunately, Hyeon, et al. have reported the synthesis of zinc oxide and silica oxide nanoparticles by a similar method to that used for the synthesis of the iron oxide particles.<sup>36-38</sup> So, if none of the ligand exchange experiments with oleic acid on iron oxide works, we also have the option of replacing iron oxide nanoparticles with some other metal oxide nanoparticles that will allow ligand exchange with shorter ligands.

After the successful self-assembly of above designed homo- and hetero- dimers and trimers, characterization becomes the next challenge, as those dimers and trimers are only about the size of 20 nm. TEM is the primary characterization tool because it presents images of the actual particles. Moreover, a series of accessorial characterization methods may also be used to provide different information of such structures indirectly. For example, IR can be employed for the identification of different capping ligands and their binding status (e.g.

bounded versus unbounded), and UV can be used for a qualitative measurement to assess the maximum particle size in solution as the optical absorbance of a nanoparticle is known to red-shift as it increases in size. This shift, however, only occurs for particles in the quantum size restricted limit and stops after the particles are only a few nanometers in size. Thus, this technique can be used to either determine the maximum particle size on larger particles, or to demonstrate that the particles in solution are below the cut-off size. Other techniques like size exclusion chromatography (SEC) are still under development by other group members working on this project, and may potentially be applicable if appropriate analytical methods can be developed using them.

At the same time, our group is also collaborating with Dr. Parson's group from the Chemical Engineering Department on testing the electronic properties of these synthesized homo- and hetero- dimers and trimers in nano-trenches. Our previous collaborations have resulted in three papers.<sup>39-41</sup> For example, one recently published paper demonstrated the conducting behavior of homo-dimer in a metal nano-trench: despite the highly conjugated, electron delocalized system in OPE linker, its conductance is still expected to be considerably lower than that of metals, where electrons flow freely, thus giving a smaller current for this homo-dimer, compared to two directly connected gold nanoparticles (Figure 25).<sup>41</sup> The same studies are yet to be conducted on hetero-dimers, homo-trimers, and hetero-trimers in future.

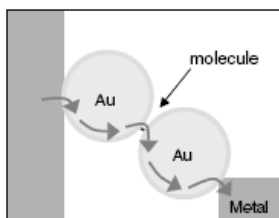


**Figure 25.** Figure from reference paper: schematic drawing showing the current flow through homo-dimer.<sup>41</sup>

### 3.5 Experimental Section

#### General Considerations

All chemicals were purchased from Aldrich or Acros.

**Synthesis of 1.** To a sealed flask containing a mixture of 8.6 mL (91.1 mmol) of *t*-BuOH and 7.4 mL (91.1 mmol) of pyridine under nitrogen protection, 10.0 g (45.6 mmol) of 4-bromobenzoyl chloride dissolved in 50 mL of DCM was added drop wise. The reaction mixture was stirred overnight at RT, and then the solid phase was filtered and discarded. The liquid layer was washed with 2M NaOH, 2M HCl, and brine, then dried over anhydrous sodium sulfate. Removal of solvent under reduced pressure gave a light yellow liquid with a small amount of solid impurities. This liquid was filtered through a small amount of celite on a fritted funnel to separate the impurities. Further drying under vacuum for 2 h gave a light yellow oily liquid (10.1 g, 86% yield). <sup>1</sup>H-NMR (CDCl<sub>3</sub>): 1.56 (s, 9H), 7.51 (d, 2H), 7.81 (d, 2H).

**Synthesis of 2.** To a Schlenk flask containing a mixture of 7.3 mg (0.007 mmol) of Pd<sub>2</sub>(dba)<sub>3</sub>, 13.3 mg (0.07 mmol) of CuI, and 18.4 mg (0.07 mmol) of PPh<sub>3</sub>, 0.47 mL (4.6

mmol) of 2-methylbut-3-yn-2-ol dissolved in 3 mL of pyridine was added slowly under nitrogen protection. To this mixture, 1.2 g (4.7 mmol) of **1** dissolved in 6 mL of triethylamine was added slowly under nitrogen protection. The reaction was stirred in this sealed Schlenk flask in an oil bath set to 100 °C for 72 h. Then the dark brown mixture was filtered through a small amount of celite on a fritted funnel to give a yellow liquid, which was washed with dilute HCl and dried over anhydrous sodium sulfate. Column purification with hexane and gradient addition of ethyl acetate, followed by removal of solvent and further drying under vacuum gave light yellow crystals (1.2 g, 98% yield). Alternatively, this reaction was carried out on a larger scale (8.8 g, 75% yield), when the column purification step was replaced by filtering through a small amount of silica on a fritted funnel. <sup>1</sup>H-NMR (CDCl<sub>3</sub>): 1.60 (s, 9H), 1.64 (s, 6H), 2.04 (s, 1H), 7.45 (d, 2H), 7.92 (d, 2H).

**Synthesis of 3.** To a flask containing 10.4 g (40.0 mmol) of **2** dissolved in 300 mL of dry toluene, 4.8 g (120.0 mmol) of sodium hydroxide powder was added. The mixture was stirred under reflux in an oil bath for 72 h. Then the solid phase was filtered and discarded. Removal of solvent under reduced pressure gave light yellow crystals (8.0 g, 99% yield). <sup>1</sup>H-NMR (CDCl<sub>3</sub>): 1.60 (s, 9H), 3.22 (s, 1H), 7.53 (d, 2H), 7.95 (d, 2H).

**Synthesis of 4a.** To a flask containing a mixture of 227.5 mg (3.5 mmol) of zinc dust and 0.43 mL (3.5 mmol) of dichlorodimethylsilane dissolved in 10 mL of 1,2-dichloroethane, a mixture of 302.5 mg (1.0 mmol) of 4-iodobenzene-1-sulfinyl chloride and 0.28 mL (3.0 mmol) of dimethylacetamide dissolved in 10 mL of 1,2-dichloroethane was added drop wise, and stirred in an oil bath set to 75 °C for 1.5 h. Then 75.9 mg (0.55 mmol) of potassium carbonate was added to this mixture and stirred in an oil bath set to 75 °C for an additional 30

min. After the solution was cooled down to RT, 0.28 mL (4.0 mmol) of acetyl chloride was added slowly and the resulting mixture was stirred overnight. Column purification with hexane and gradient addition of ethyl acetate, followed by removal of solvent and further drying under vacuum gave a yellow solid (166.4 mg, 60% yield). <sup>1</sup>H-NMR (CDCl<sub>3</sub>): 2.39 (s, 3H), 7.11 (d, 2H), 7.71 (d, 2H).

**Synthesis of 4b.** A flask containing a mixture of 1.9 mL (20.0 mmol) of acetic anhydride and 1.4 mL of 88% formic acid was heated to 60 °C for 30 min, and then cooled down in an ice bath. 2.2 g (10.0 mmol) of 4-iodoaniline dissolved in 5 mL of THF was added slowly into this solution, and stirred at RT overnight to give a light brown mixture. Solvent was removed under reduced pressure. At the addition of DI, a light grey solid precipitated out. This solid was washed by DI and dried under vacuum. Recrystallization in DCM/hexane (1:1) gave white crystals (1.4 g, 57% yield). <sup>1</sup>H-NMR (CDCl<sub>3</sub>): 6.87 (d, 1H), 7.34 (d, 2H), 7.66 (t, 3H), 8.40 (s, 1H), 8.66 (d, 1H).

**Synthesis of 5a.** To a Schlenk flask containing a mixture of 76.5 mg (0.07 mmol) of Pd<sub>2</sub>(dba)<sub>3</sub>, 93.6 mg (0.5 mmol) of CuI, and 129.1 mg (0.5 mmol) of PPh<sub>3</sub>, a mixture of 1.0 g (5.0 mmol) of **3** and 1.4 g (5.0 mmol) of **4a** dissolved in 30 mL of triethylamine was added slowly under nitrogen protection. The reaction was stirred in this sealed Schlenk flask in an oil bath set to 65 °C for 72 h. Then the dark brown mixture was purified by filtering through a small amount of celite on a fritted funnel to give a yellow liquid. This liquid was washed with dilute HCl and dried over anhydrous sodium sulfate. Column purification with hexane and gradient addition of ethyl acetate, followed by removal of solvent and further drying under vacuum gave a yellow solid (1.5 g, 86% yield). <sup>1</sup>H-NMR (CDCl<sub>3</sub>): 1.61 (s, 9H), 2.45

(s, 3H), 7.43 (d, 2H), 7.59 (q, 4H), 7.98 (d, 2H).

**Synthesis of 5b.** To a Schlenk flask containing a mixture of 76.5 mg (0.07 mmol) of  $\text{Pd}_2(\text{dba})_3$ , 93.6 mg (0.5 mmol) of  $\text{CuI}$ , and 129.1 mg (0.5 mmol) of  $\text{PPh}_3$ , a mixture of 1.0 g (5.0 mmol) of **3** and 1.2 g (5.0 mmol) of **4b** dissolved in 15 mL of triethylamine and 15 mL of THF was added slowly under nitrogen protection. The reaction was stirred in this sealed Schlenk flask in an oil bath set to 65 °C for 72 h. Then the dark brown mixture was purified by filtering through a small amount of celite on a fritted funnel to give a yellow liquid. This liquid was washed with dilute HCl and dried over anhydrous sodium sulfate. Column purification with hexane and gradient addition of ethyl acetate, followed by removal of solvent and further drying under vacuum gave a yellow solid (1.0 g, 62% yield).  $^1\text{H-NMR}$  ( $\text{CDCl}_3$ ): 1.61 (s, 9H), 7.09 (d, 2H), 7.57 (q, 4H), 7.97 (d, 2H), 8.42 (s, 1H).

**Synthesis of 6b.** To a flask containing a mixture of 96.3 mg (0.3 mmol) of **5b** and 89.1 mg (0.3 mmol) of triphosgene under nitrogen protection, a mixture of 3 mL of triethylamine and 6 mL of DCM was added slowly. Then 6.8 mg (0.03 mmol) of benzyltriethylammonium chloride dissolved in 4 mL of DCM was added. The reaction mixture was stirred in an oil bath set to 40 °C for 48 h, and then the dark brown mixture was purified by filtering through a small amount of celite on a fritted funnel to give a yellow liquid. This liquid was washed with DI and brine, and dried over anhydrous sodium sulfate. Column purification with hexane and gradient addition of ethyl acetate, followed by removal of solvent and further drying under vacuum gave light brown crystals (77.0 mg, 85% yield).  $^1\text{H-NMR}$  ( $\text{CDCl}_3$ ): 1.61 (s, 9H), 7.38 (q, 4H), 7.57 (d, 2H), 7.99 (d, 2H).

**Synthesis of 7a.** To a flask containing 1.0 g (2.8 mmol) of **5a**, 0.88 mL (11.2 mmol) of

trifluoroacetic acid was added and stirred at RT under nitrogen protection for 48 h. Removal of solvent under reduced pressure gave an off-white solid. This solid was washed with hexane and dried under vacuum to give a light yellow solid (0.57 g, 68% yield).  $^1\text{H-NMR}$  (DMSO): 2.43 (s, 3H), 7.46 (d, 2H), 7.65 (t, 4H), 7.95 (d, 2H).  $^{13}\text{C-NMR}$  (DMSO): 30.96, 90.74, 91.68, 123.45, 126.80, 129.56, 130.20, 131.53, 132.28, 132.82, 135.14, 167.31, 193.53.

**Synthesis of 7b.** To a flask containing 0.8 g (2.6 mmol) of **6b** dissolved in 20 mL of DCM, 3.0 g (13.2 mmol) of zinc bromide powder was added and stirred at RT under nitrogen protection for 24 h. Then 200 mL of DI was added to the reaction mixture and stirred for an additional 2 h. The whole solution was then washed with DCM. Removal of solvent from combined DCM layers under reduced pressure gave a brown solid. This solid was washed with hot ethanol and cold DCM to give a light brown solid (451.6 mg, 70% yield).  $^1\text{H-NMR}$  (DMSO): 7.64 (d, 2H), 7.67 (q, 4H), 7.95 (d, 2H). IR:  $1689\text{ cm}^{-1}$  (CO),  $2119\text{ cm}^{-1}$  (NC). MS: 248 (in acidic solution).

**Synthesis of 8.** To a flask containing 25.0 g (0.45 mol) of potassium hydroxide dissolved in 200 mL of anhydrous ethanol at RT under nitrogen protection, 19.3 g (0.18 mol) of hydroquinone dissolved in 75 mL of anhydrous ethanol was added drop wise, after which 74.0 g (0.45 mol) of 1-bromohexane dissolved in 25 mL of anhydrous ethanol was added slowly. The whole mixture was then stirred under reflux at  $100\text{ }^\circ\text{C}$  overnight under nitrogen protection. After removal of most ethanol, 250 mL of DI was added to the residue, and extracted with ethyl acetate. The ethyl acetate layer was washed with DI and brine, and dried over anhydrous sodium sulfate. Removal of solvent under reduced pressure gave an off-white

solid. This solid was recrystallized from hot ethanol to give white crystals (43.0 g, 88% yield). <sup>1</sup>H-NMR (CDCl<sub>3</sub>): 0.92 (t, 6H), 1.35 (q, 8H), 1.45 (p, 4H), 1.75 (p, 4H), 3.91 (t, 4H), 6.83 (s, 4H).

**Synthesis of 9.** To a flask containing 11.1 g (40.0 mmol) of **8** dissolved in a mixture of 90 mL of acetic acid, 7 mL of DI, and 3 mL of concentrated sulfuric acid, a mixture of 10.3 g (48.0 mmol) of potassium iodate and 13.1 g (48.0 mmol) of iodine dissolved in 50 mL of acetic acid was added slowly, and stirred in an oil bath set to 70 °C for 24 h. To this reaction mixture, 20% sodium sulfite solution was added till the brown color of iodine disappeared. Then the mixture was poured slowly into ice water with sodium sulfite, extracted with hexane, washed with brine, and dried over anhydrous sodium sulfate. Removal of solvent under reduced pressure and recrystallization from hot ethanol gave light yellow crystals (16.0 g, 76% yield). <sup>1</sup>H-NMR (CDCl<sub>3</sub>): 0.92 (t, 6H), 1.25 (h, 4H), 1.35 (p, 4H), 1.45 (p, 4H), 1.78 (p, 4H), 3.93 (t, 4H), 7.19 (s, 2H).

**Synthesis of 10.** To a Schlenk flask containing a mixture of 31.1 mg (0.03 mmol) of Pd<sub>2</sub>(dba)<sub>3</sub>, 19.1 mg (0.1 mmol) of CuI, and 26.2 mg (0.1 mmol) of PPh<sub>3</sub>, 0.71 mL (7.0 mmol) of 2-methylbut-3-yn-2-ol dissolved in 5 mL of pyridine was added slowly under nitrogen protection. To this mixture, 5.3 g (10.0 mmol) of **9** dissolved in 20 mL of triethylamine was added slowly under nitrogen protection. The reaction was stirred in this sealed Schlenk flask in an oil bath set to 65 °C for 48 h, after which the dark brown mixture was purified by filtering through a small amount of celite on a fritted funnel to give a dark yellow liquid. This liquid was washed with 0.01 M HCl and dried over anhydrous sodium sulfate. Column purification with hexane and gradient addition of ethyl acetate, followed by removal of

solvent and further drying under vacuum gave a dark brown oily liquid (3.1 g, 92% yield). <sup>1</sup>H-NMR (CDCl<sub>3</sub>): 0.92 (t, 6H), 1.35 (p, 8H), 1.45 (p, 4H), 1.80 (p, 4H), 2.04 (s, 1H), 3.94 (t, 4H), 6.81 (s, 1H), 7.29 (s, 1H).

**Synthesis of 11.** To a Schlenk flask containing a mixture of 77.6 mg (0.07 mmol) of Pd<sub>2</sub>(dba)<sub>3</sub>, 95.3 mg (0.5 mmol) of CuI, and 131.0 mg (0.5 mmol) of PPh<sub>3</sub>, a mixture of 2.4 g (5.0 mmol) of **10** and 1.0 g (5.0 mmol) of **3** was added slowly under nitrogen protection. The reaction was stirred in this sealed Schlenk flask in an oil bath set to 80 °C for 72 h, after which the dark brown mixture was purified by filtering through a small amount of celite on a fritted funnel to give a dark yellow liquid. This liquid was washed with 0.2 M HCl and dried over anhydrous sodium sulfate. Column purification with hexane and gradient addition of ethyl acetate, followed by removal of solvent and further drying under vacuum gave a dark brown oily liquid (3.4 g, 96% yield). <sup>1</sup>H-NMR (CDCl<sub>3</sub>): 0.82 (p, 6H), 1.13-1.74 (25H), 3.21 (s, 1H), 3.90 (t, 4H), 6.83 (s, 1H), 6.88 (s, 1H), 7.50 (d, 2H), 7.88 (d, 2H).

**Synthesis of 12.** To a tube containing 56.0 mg (0.1 mmol) of **11** dissolved in 3 mL of dry toluene, 12.0 mg (0.3 mmol) of sodium hydroxide powder was added and stirred at 150 °C in a microwave reactor for 20 min. Then the solid phase was filtered and discarded, while the liquid phase was washed with 0.2 M HCl. Removal of solvent under reduced pressure gave a yellow solid (48.6 mg, 97% yield). <sup>1</sup>H-NMR (CDCl<sub>3</sub>): 0.91 (p, 6H), 1.33-1.53 (12H), 1.61 (s, 9H), 1.83 (p, 4H), 3.37 (s, 1H), 4.01 (t, 4H), 6.99 (s, 1H), 7.03 (s, 1H), 7.57 (d, 2H), 7.97 (d, 2H).

**Synthesis of 13a.** To a Schlenk flask containing a mixture of 76.5 mg (0.07 mmol) of Pd<sub>2</sub>(dba)<sub>3</sub>, 93.6 mg (0.5 mmol) of CuI, and 129.1 mg (0.5 mmol) of PPh<sub>3</sub>, a mixture of 1.0 g

(5.0 mmol) of **3** and 1.4 g (5.0 mmol) of **4a** dissolved in 30 mL of triethylamine was added slowly under nitrogen protection. The resulting mixture was stirred in this sealed Schlenk flask in an oil bath set to 65 °C for 72 h, and then the dark brown mixture was purified by filtering through a small amount of celite on a fritted funnel to give a yellow liquid. This liquid was washed with dilute HCl and dried over anhydrous sodium sulfate. Column purification with hexane and gradient addition of ethyl acetate, followed by removal of solvent and further drying under vacuum gave a yellow solid (1.5 g, 86% yield). <sup>1</sup>H-NMR (CDCl<sub>3</sub>): 0.92 (p, 6H), 1.25-1.42 (8H), 1.56 (h, 4H), 1.61 (s, 9H), 1.85 (p, 4H), 2.45 (s, 3H), 4.04 (t, 4H), 7.03 (s, 2H), 7.42 (d, 2H), 7.58 (q, 4H), 7.96 (d, 2H).

**Synthesis of 13b.** To a Schlenk flask containing a mixture of 15.6 mg (0.015 mmol) of Pd<sub>2</sub>(dba)<sub>3</sub>, 19.0 mg (0.1 mmol) of CuI, and 26.2 mg (0.1 mmol) of PPh<sub>3</sub>, a mixture of 502.0 mg (1.0 mmol) of **12** and 247.0 mg (1.0 mmol) of **4b** dissolved in 5 mL of triethylamine and 10 mL of THF was added slowly under nitrogen protection. The reaction mixture was stirred in this sealed Schlenk flask in an oil bath set to 65 °C for 72 h, and then the dark brown mixture was purified by filtering through a small amount of celite on a fritted funnel to give a yellow liquid. This liquid was washed with dilute HCl and dried over anhydrous sodium sulfate. Column purification with hexane and gradient addition of ethyl acetate followed by removal of solvent and further drying under vacuum gave a yellow solid (475.6 mg, 77% yield). <sup>1</sup>H-NMR (CDCl<sub>3</sub>): 0.91 (p, 6H), 1.26-1.58 (12H), 1.61 (s, 9H), 1.86 (p, 4H), 4.04 (t, 4H), 7.02 (s, 2H), 7.55 (q, 4H), 7.97 (d, 2H), 8.42 (d, 2H), 8.75 (d, 1H).

**Synthesis of 14b.** To a flask containing a mixture of 850.0 mg (1.4 mmol) of **13b** and 407.0 mg (1.4 mmol) of triphosgene under nitrogen protection, a mixture of 2 mL of

triethylamine and 12 mL of DCM was added slowly. Then 31.0 mg (0.14 mmol) of benzyltriethylammonium chloride dissolved in 8 mL of DCM was added to this mixture, and stirred in an oil bath set to 40 °C for 48 h. Then the dark brown reaction mixture was purified by filtering through a small amount of celite on a fritted funnel to give a yellow liquid. This liquid was washed with DI and brine, and then dried over anhydrous sodium sulfate. Column purification with hexane and gradient addition of ethyl acetate, followed by removal of solvent and further drying under vacuum gave a light brown solid (801.7 mg, 97% yield). <sup>1</sup>H-NMR (CDCl<sub>3</sub>): 0.91 (p, 6H), 1.26-1.58 (12H), 1.61 (s, 9H), 1.87 (p, 4H), 4.04 (t, 4H), 7.03 (s, 2H), 7.31 (d, 2H), 7.52 (q, 4H), 8.05 (d, 2H).

**Synthesis of 15a.** To a flask containing 146.3 mg (0.2 mmol) of **13a**, 0.07 mL (0.8 mmol) of trifluoroacetic acid was added and stirred at RT under nitrogen protection for 48 h. Solvent was removed under reduced pressure, and the remaining solid was re-dissolving into acetonitrile. At the addition of DI, a yellow solid precipitated out. This solid was filtered and dried under vacuum to give a yellow solid (93.6 mg, 70% yield). However, this product is not stable in air and can fully decompose within several days. Practically, it is better to stock this in the form of **13a**, and only deprotect the *tert*-butyl group when ready to use. <sup>1</sup>H-NMR (CDCl<sub>3</sub>): 0.90 (p, 6H), 1.26-1.58 (12H), 1.85 (p, 4H), 2.45 (s, 3H), 4.04 (t, 4H), 7.03 (d, 2H), 7.43 (d, 2H), 7.62 (q, 4H), 8.06 (d, 2H). <sup>13</sup>C-NMR (CDCl<sub>3</sub>): 14.21, 22.81, 25.91, 29.87, 31.75, 69.79, 94.52, 117.08, 124.84, 129.01, 130.28, 131.68, 132.30, 134.36, 154.01, 193.30. IR: 1694 cm<sup>-1</sup> (CO). MS: 597 (in acidic solution).

**Synthesis of 15b.** To a flask containing 250 mg (0.4 mmol) of **14b** dissolved in 8 mL of DCM, 466.0 mg (2.0 mmol) of zinc bromide powder was added and stirred at RT under

nitrogen protection for 24 h. Then 50 mL of DI was added to the reaction mixture and stirred for an additional 2 h. This reaction mixture was washed with DCM several times, and the solvent was removed from combined DCM layers under reduced pressure to give a dark brown solid. This solid was washed with hot ethanol and cold DCM to give a brown solid (~90 mg, ~40% yield). However, this product is highly unstable and starts to decompose immediately, that even after drying under vacuum for 30 min, the NMR shows considerable impurities. Practically, it is better to stock this in the form of **14b** and only deprotect the *tert*-butyl group when ready to use. <sup>1</sup>H-NMR (CDCl<sub>3</sub>): 0.91 (p, 6H), 1.26-1.38 (12H), 1.87 (p, 4H), 4.04 (t, 4H), 7.03 (s, 2H), 7.53 (d, 2H), 7.62 (q, 4H), 8.08 (d, 2H). IR: 1689 cm<sup>-1</sup> (CO), 2119 cm<sup>-1</sup> (NC).

**Synthesis of hexanethiol capped gold nanoparticles.** To a flask containing a mixture of 30 mL of 30 mM HAuCl<sub>4</sub>·3H<sub>2</sub>O (aq.) and 80 mL of 50 mM tetraoctylammonium bromide dissolved in toluene, 0.12 mL (0.8 mmol) of hexanethiol dissolved in DI was added and stirred vigorously for a few minutes. Then 25 mL of 0.4 M sodium borohydride was added slowly and stirred overnight at RT. Acetone was added to the organic phase to precipitate out the desired particles. These particles were washed with acetone and ethanol, and then re-dissolved into toluene to give a well-dispersed, dark red solution.

**Synthesis of hexanethiol capped platinum nanoparticles.** To a flask containing 0.47 g (1.1 mmol) of H<sub>2</sub>PtCl<sub>6</sub> dissolved in 35 mL of anhydrous THF under nitrogen protection, 0.13 mL (0.9 mmol) of hexanethiol was added and stirred for 30 min. Then 22 mL of 1 M super-hydride (LiTEBH) was added drop wise. The reaction mixture was stirred overnight at RT. Then methanol was added slowly to quench LiTEBH, after which the desired particles

were precipitated out and washed with ethanol, and then re-dissolved into toluene to give a well-dispersed, dark brown solution.

## REFERENCES

- (1) Campbell, L. M.; Dixon, D. G.; Hecky, R. E. *Journal of Toxicology and Environmental Health-Part B-Critical Reviews* **2003**, *6*, 325-356.
- (2) Ha-Thi, M. H.; Penhoat, M.; Michelet, V.; Leray, I. *Org. Lett.* **2007**, *9*, 1133-1136.
- (3) Atwood, D. A. *Recent Developments in Mercury Science*; Springer, 2006; Vol. 120.
- (4) Cai, Y. *Biogeochemistry of Environmentally Important Trace Elements* **2003**, *835*, 1-10.
- (5) Miao, S. B.; Bangcuyo, C. G.; Smith, M. D.; Bunz, U. H. F. *Angew. Chem.-Int. Edit.* **2006**, *45*, 661-665.
- (6) Huang, C. C.; Chang, H. T. *Chem. Commun.* **2007**, 1215-1217.
- (7) Li, M. J.; Chu, B. W. K.; Zhu, N. Y.; Yam, V. W. W. *Inorg. Chem.* **2007**, *46*, 720-733.
- (8) Wakabayashi, S.; Kato, Y.; Mochizuki, K.; Suzuki, R.; Matsumoto, M.; Sugihara, Y.; Shimizu, M. *J. Org. Chem.* **2007**, *72*, 744-749.
- (9) Caballero, A.; Lloveras, V.; Curiel, D.; Tarraga, A.; Espinosa, A.; Garcia, R.; Vidal-Gancedo, J.; Rovira, C.; Wurst, K.; Molina, P.; Veciana, J. *Inorg. Chem.* **2007**, *46*, 825-838.
- (10) Ho, I. T.; Lee, G. H.; Chung, W. S. *J. Org. Chem.* **2007**, *72*, 2434-2442.
- (11) Hong Yang, Z.-G. Z., Jia Xu, Fu-You Li, Tao Yi, and Chun-Hui Huang. *Tetrahedron* **2007**, *63*, 6732-6736.
- (12) Batista, R. M. F.; Oliveira, E.; Costa, S. P. G.; Lodeiro, C.; Raposo, M. M. M. *Org. Lett.* **2007**, *9*, 3201-3204.
- (13) Yoon, S.; Miller, E. W.; He, Q.; Do, P. H.; Chang, C. J. *Angew. Chem.-Int. Edit.* **2007**, *46*, 6658-6661.
- (14) Lee, J. S.; Han, M. S.; Mirkin, C. A. *Angew. Chem.-Int. Edit.* **2007**, *46*, 4093-4096.
- (15) Liu, X. F.; Tang, Y. L.; Wang, L. H.; Zhang, J.; Song, S. P.; Fan, C.; Wang, S. *Adv. Mater.* **2007**, *19*, 1471-+.
- (16) Soh, J. H.; Swamy, K. M. K.; Kim, S. K.; Kim, S.; Lee, S. H.; Yoon, J. *Tet. Lett.* **2007**, *48*, 5966-5969.

- (17) Lee, M. H.; Cho, B. K.; Yoon, J.; Kim, J. S. *Org. Lett.* **2007**, *9*, 4515-4518.
- (18) Frohn, M.; Burli, R. W.; Riahi, B.; Hungate, R. W. *Tetrahedron Lett.* **2007**, *48*, 487-489.
- (19) F. A. Cotton, G. W. *Advanced Inorganic Chemistry*; 6th ed., 1999.
- (20) van den Ancker, T. R.; Engelhardt, L. M.; Henderson, M. J.; Jacobsen, G. E.; Raston, C. L.; Skelton, B. W.; White, A. H. *Journal of Organometallic Chemistry* **2004**, *689*, 1991-1999.
- (21) Feynman, R. P. *Engineering and Science* **1960**, *XXIII*.
- (22) Tour, J. M.; Rawlett, A. M.; Kozaki, M.; Yao, Y. X.; Jagessar, R. C.; Dirk, S. M.; Price, D. W.; Reed, M. A.; Zhou, C. W.; Chen, J.; Wang, W. Y.; Campbell, I. *Chem.-Eur. J.* **2001**, *7*, 5118-5134.
- (23) Laibinis, P. E.; Hickman, J. J.; Wrighton, M. S.; Whitesides, G. M. *Science* **1989**, *245*, 845-847.
- (24) Hickman, J. J.; Laibinis, P. E.; Auerbach, D. I.; Zou, C. F.; Gardner, T. J.; Whitesides, G. M.; Wrighton, M. S. *Langmuir* **1992**, *8*, 357-359.
- (25) Walker, B. R.; Wassel, R. A.; Stefanescu, D. M.; Gorman, C. B. *J. Am. Chem. Soc.* **2004**, *126*, 16330-16331.
- (26) Dadosh, T.; Gordin, Y.; Krahne, R.; Khivrich, I.; Mahalu, D.; Frydman, V.; Sperling, J.; Yacoby, A.; Bar-Joseph, I. *Nature* **2005**, *436*, 1200-1200.
- (27) Brousseau, L. C.; Novak, J. P.; Marinakos, S. M.; Feldheim, D. L. *Adv. Mater.* **1999**, *11*, 447-+.
- (28) Tour, J. M. *Chem. Rev.* **1996**, *96*, 537-553.
- (29) Wu, J. S.; Chi, C. Y.; Wang, X. H.; Li, J.; Zhao, X. J.; Wang, F. S. *Synth. Commun.* **2000**, *30*, 4293-4298.
- (30) Wu, Y. Q.; Limburg, D. C.; Wilkinson, D. E.; Vaal, M. J.; Hamilton, G. S. *Tet. Lett.* **2000**, *41*, 2847-2849.
- (31) Chang, C. Y. *Proc. IEEE* **2003**, *91*, 1756-1764.
- (32) Eklund, S. E.; Cliffel, D. E. *Langmuir* **2004**, *20*, 6012-6018.
- (33) Hyeon, T.; Lee, S. S.; Park, J.; Chung, Y.; Bin Na, H. *J. Am. Chem. Soc.* **2001**, *123*, 12798-12801.

- (34) Brust, M.; Walker, M.; Bethell, D.; Schiffrin, D. J.; Whyman, R. *J. Chem. Soc.-Chem. Commun.* **1994**, 801-802.
- (35) Zamborini, F. P.; Gross, S. M.; Murray, R. W. *Langmuir* **2001**, *17*, 481-488.
- (36) Joo, J.; Kwon, S. G.; Yu, J. H.; Hyeon, T. *Adv. Mater.* **2005**, *17*, 1873-1877.
- (37) Choi, S. H.; Kim, E. G.; Park, J.; An, K.; Lee, N.; Kim, S. C.; Hyeon, T. *J. Phys. Chem. B* **2005**, *109*, 14792-14794.
- (38) Park, J.; Kang, E. A.; Bae, C. J.; Park, J. G.; Noh, H. J.; Kim, J. Y.; Park, J. H.; Park, J. H.; Hyeon, T. *J. Phys. Chem. B* **2004**, *108*, 13594-13598.
- (39) Ezell, R. G.; Gorman, I.; Lokitz, B.; Ayres, N.; McCormick, C. L. *J. Polym. Sci. A, Polym. Chem.* **2006**, *44*, 3125-3139.
- (40) Chu, C.; Ayres, J. A.; Stefanescu, D. M.; Walker, B. R.; Gorman, C. B.; Parsons, G. N. *J. Phys. Chem. C* **2007**, *111*, 8080-8085.
- (41) Na, J. S.; Ayres, J.; Chandra, K. L.; Chu, C.; Gorman, C. B.; Parsons, G. N. *Nanotechnology* **2007**, *18*, -.